MICROFABRICATED THIN SILICON VAPOR CHAMBERS FOR LOW PROFILE THERMAL MANAGEMENT

A Dissertation
Presented to
The Academic Faculty

by

Jiaxing Liang

In Partial Fulfillment
of the Requirements for the Degree
'Master of Science' in the
GEORGE W. WOODRUFF SCHOOL OF MECHANICAL ENGINEERING
COLLEGE OF ENGINEERING

Georgia Institute of Technology
August 2017

MICROFABRICATED THIN SILICON VAPOR CHAMBERS FOR LOW PROFILE THERMAL MANAGEMENT

Approved by:

Dr. Yogendra Joshi
School of Mechanical Engineering
Georgia Institute of Technology

Dr. Muhannad S Bakir
School of Electrical and Computer Engineering
Georgia Institute of Technology

Dr. Suresh K. Sitaraman
School of Mechanical Engineering
Georgia Institute of Technology

Date Approved: May 2, 2017

ACKNOWLEDGEMENTS

I want to thank you for the DARPA IceCool Applications program for funding and supporting this project.

I want to thank you, my two co-advisors, Prof. Yogendra Joshi and Prof. Muhannad S Bakir, for giving me a lot of supports, suggestions, and comments on the project. We together made efforts to accomplish the project. I want to thank you, my undergraduate advisor Prof. Suresh K. Sitaraman, for recommending me to Prof. Yogendra Joshi and gave me supports in the beginning of my graduate study.

I want to thank you, Zhimin wan, Xuchen Zhang, Thomas Sarvey and Georgia Tech cleanroom staffs, for their help in cleanroom fabrication.

I want to thank you, Drs. Peter de Bock and Joo Kim from General Electric Global Research, for giving suggestions on the design of the vapor chamber charging station.

I want to thank you, Sangbeom Cho, for working together in constructing the charging station, and thank you all METTL group members for their help and suggestions.

I want to thank you, my friend Yaqin song, for taking those nice SEM photos.

I want to thank you, my girlfriend, for always supporting me in my life.

Lastly, I want to thank you my Dad and my Mom and my family so much for always supporting and encouraging me in my life.

TABLE OF CONTENTS

LIST OF TABLES

LIST OF FIGURES

LIST OF SYMBOLS AND ABBREVIATIONS

A_v	Vapor space cross-sectional area
A_{wick}	Wick cross-section area
C	Mach number dependent constant
d	diameter
d_{eff}	Effective capillary diameter
d_v	Diameter of vapor space
f_v	Vapor drag coefficient
g	Gravitation acceleration
h	Meniscus height
H	Normalized meniscus height
$h_{eff,evap}$	Effective heat transfer coefficient of evaporation
$h_{eff,wick}$	Effective heat transfer coefficient of wick
$h_{eff,HP}$	Effective heat transfer coefficient of heat pipe
h_{fg}	Latent heat of vaporization
$k_{cluster}$	Thermal conductivity of cluster
$k_{eff,HP}$	Effective thermal conductivity of heat pipe
$k_{eff,VC}$	Effective thermal conductivity of vapor chamber
k_l	Thermal conductivity of liquid phase
k_s	Thermal conductivity of solid phase
k_{wick}	Thermal conductivity of wick
K	Permeability
L	Length

L_{adia}	Length of adiabatic section
L_{cond}	Length of condensation section
L_{eff}	Effective length
L_{evap}	Length of evaporation section
M_v	Vapor Mach number
ID	Inner diameter
p	Pitch
P	Normalized pitch
ΔP_c	Capillary pressure
ΔP_{cond}	Capillary pressure at condenser
ΔP_{evap}	Capillary pressure at evaporator
ΔP_g	Pressure drop due to gravity
ΔP_l	Liquid pressure drop
ΔP_{nor}	Normalized capillary pressure
ΔP_v	Vapor pressure drop
$\Delta P_{\|\|}$	Axial hydrostatic pressure drop
$\Delta P_{\perp}$	Normal hydrostatic pressure drop
q	Power
$q"$	Heat flux
r	Radius
r_{cond}	Effective capillary radius at condenser
r_{eff}	Effective capillary radius
r_{evap}	Effective capillary radius at evaporator
r_{hv}	Hydraulic radius of vapor space

R_{evap}	Thermal resistance of evaporator
R_v	Vapor gas constant
R_{wick}	Thermal resistance of wick
R_{HP}	Thermal resistance of heat pipe
R_{VC}	Thermal resistance of vapor chamber
Re_v	Vapor Reynolds number
S	Spacing
T_v	Vapor temperature

Greek symbols

σ	Surface tension
γ_v	Vapor specific heat ratio
ε	Porosity
θ	Contact angle (CA)
μ_l	Liquid viscosity
μ_v	Vapor dynamic viscosity
ρ_l	Liquid density
ρ_v	Vapor density
ψ	Inclination angle

SUMMARY

Portable electronics, such as smartphones, tablets, and ultrabooks are innovating rapidly. They are becoming as powerful as desktop computers, and incorporating multiple functionalities enabled through three-dimensional electronics, or 2.5-dimensional interposer based packaging approaches. To keep these compact electronic systems operating efficiently and reliably, thermal management becomes a challenging problem. A proposed solution is to develop miniature thermal management devices suitable for integration into small form factor packages, incorporating silicon interposers, or three-dimensional packaging. Vapor chamber is a technology that utilizes the latent heat of liquid/vapor phase change of a working liquid for heat removal, and passive capillary action to return the condensed liquid to the heat source. The main goal of this study is to develop a submillimeter thick vapor chamber that can be integrated into silicon interposer for heat spreading, and performs better than solid silicon heat spreader of the same thickness.

This study is presented in five chapters. Chapter 1 introduces the fundamentals of vapor chambers/heat pipes, and reviews recent studies on thin vapor chambers. Chapter 2 introduces the fundamentals of wick structures by reviewing recent studies, and gives numerical modeling results using Surface Evolver, and analyses selected wick structures for capillary pressure, permeability, and effective thermal conductivity. Chapter 3 provides detailed descriptions of the vapor chamber fabrication by MEMS processes, charging with a working liquid, and testing under different scenarios. Chapter 4 gives detailed discussions on the experimental results, and shows how wick saturation ratio and wick porosity can

affect the thermal performance of the vapor chamber. Also presented are the results of the extended thermal testing to see its impact on reliability. The thermal modeling results are validated with measurements. Chapter 5 concludes this study, and discusses recommended future work.

CHAPTER 1. INTRODUCTION

1.1 Thermal Management for Portable Electronics

The development of portable electronics, such as smartphones, tablets, and ultrabooks, is rapidly evolving. Current systems have significantly more functionality than those in the 1980s, and are even comparable to computers developed nowadays. Their sizes and thicknesses are significantly reduced. Even as the Moore's Law slows at the integrated circuit level, the "More-than-Moore" trend is most evident in portable electronics. Thermal management has become more challenging for portable systems, since more functionality is being integrated into increasingly smaller and thinner geometries, while stringent design constraints, such as touch temperature are imposed.

The volumetric power density increases, as more power is dissipated over a smaller volume, presenting unique challenges, as three-dimensional (3D) electronics and interposer technologies (2.5D) are pursued. Interposers provide high density interconnect substrates, that facilitate stacked chip electronics packaging. They provide interconnection between fine pitch I/Os at the die level, and coarse pitch I/Os at package level through the vertical through-silicon vias (TSVs), and multiple lateral wiring layers, called redistribution layers [1]. Figure 1 illustrates two different interposer structures. As it shows, many components are packed closely, which increases the volumetric heat generation. Inadequate thermal management can result in unacceptably high temperatures.

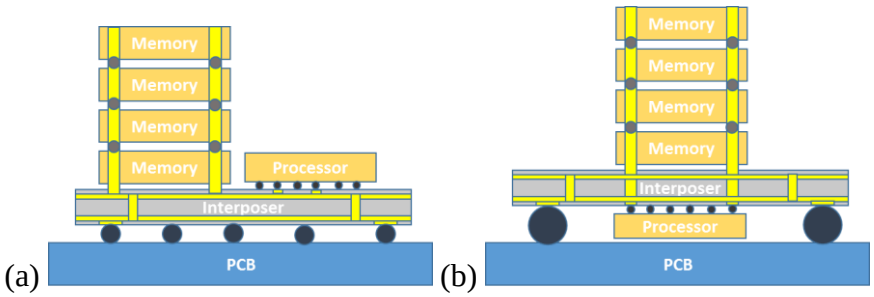

Figure 1. Two different interposer structures: (a) 2.5D interposer; (b) 3D interposer

1.2 Heat Pipe and Vapor Chamber Fundamentals and Reviews

One possible solution to the thermal management of compact, portable electronics is the heat pipe/vapor chamber technology. Heat pipe utilizes the latent heat of liquid/vapor phase change of a working fluid in the evaporator section, where the heat input from the electronic chips is applied. The vapor flow transmits heat from the heat source to the heat sink. The vapor rejects heat to the ambient in the condenser section, and the condensed liquid returns to the heated region by passive capillary pumping. Through proper design, an overall thermal resistance lower than solid heat spreaders is achieved. A typical heat pipe is shown in Figure 2. It consists of a pipe, wick structure and working fluid, and is divided into an evaporator, adiabatic and condenser section. The pipe needs to be evacuated to remove any non-condensable gasses, charged with a proper amount of the working fluid that saturates the wick structure, and hermetically sealed to function. Heat pipes can function under different orientations, but with different performance.

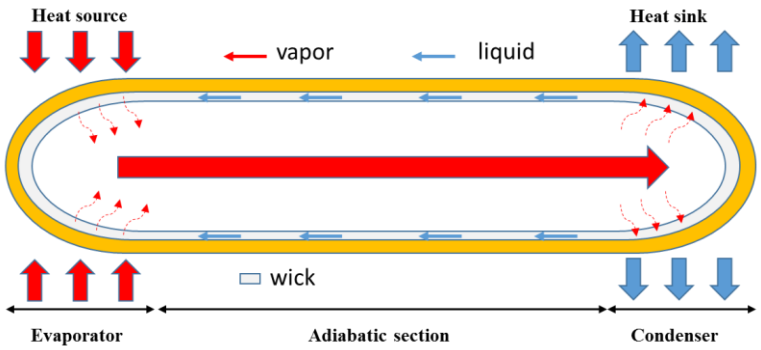

Figure 2. Fluid circulation in a heat pipe

A vapor chamber is a planar device that spreads heat two-dimensionally, while a traditional heat pipe spreads heat one-dimensionally. A vapor chamber is shown in Figure 3 with a typical heating and cooling configuration, where the heat is input at the bottom, and is rejected uniformly on the top surface.

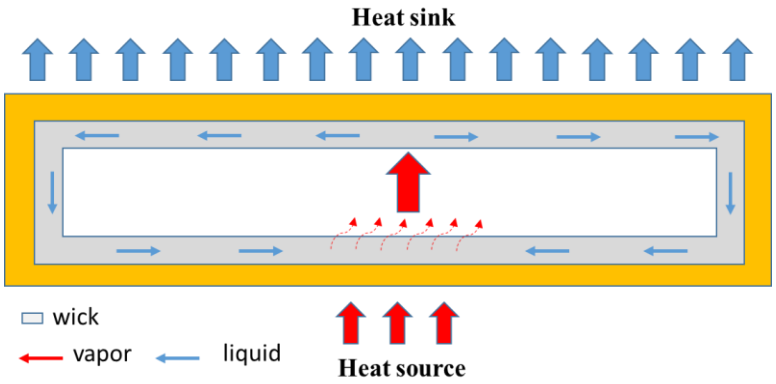

Figure 3. Vapor chamber under a typical heating cooling configuration

Silicon heat pipes and vapor chambers have been studied in recent years through experiments and modeling, due to their potentially easier integration with chips. Table 1 summarizes these studies. The thermal performance of and flow visualization in a vapor chamber with microchannels serving as wick structures was reported [2]. Vapor chambers

with different pin-fin structures were fabricated, and their performance was compared at different inclination angles. Taniguchi, et al. [3] designed and fabricated a 0.4 mm thick silicon vapor chamber with TSVs integrated for 3D electronics packaging. They showed a 7.1% improvement in thermal resistance compared to a sample without any working fluid, and observed a blocked vapor passage at TSV pitch of 200 μm during the charging process. 3 mm thick vapor chambers under different gravity conditions from Cai, et al. [4] reached an effective thermal conductivity of over 2,500 W/m-K. In a subsequent study, they reported on material and process compatibility [5].

He, et al. [6] reported on a 1.3 mm thick Au-Si eutectic bonded silicon vapor chamber that performed three times better than an uncharged sample at 15 W/cm^2 heat flux, under 15 ^oC superheat. Launay, et al. [7] studied etched micro-heat pipe arrays on silicon wafers. The micro-heat pipe arrays had microchannels with triangular cross-sections, and were integrated with liquid arteries to increase liquid flow area, and reduce liquid pressure drops. Experimental results showed that the silicon wafer with artery micro-heat pipe arrays, which were charged with methanol, had a higher effective thermal conductivity than a solid silicon benchmark. Ivanova, et al. [8] developed a 1 mm thick flat silicon heat pipe with microcapillary radial grooves, and showed a heat removal capability of 70 W at a condenser temperature of 50 ^oC without dryout.

Table 1. Designs and performance of various silicon heat pipes and vapor chambers (see Figure 4 for configuration)

Author	Working fluid	Heat Sink and configuration	Heat flux/ heat input	Thermal resistance/ effective thermal conductivity	Dimensions, mm	Vapor core thickness, µm	Wick structure	Wick size, µm
Cai, et al. [4]	ethanol	liquid cooled copper block configuration: 1	8.33 W/cm^2	2500 W/m-K 0.15 K/W	38x38x3	1500	micro-pillars	d: 10 thickness: 220
Yang, et al. [2]	water	liquid cooled block configuration: 1	~8.16 W/cm^2	~1.3 - 5.7 K/W	35x40x1.525	450	micro-channel with pin fin supports	thickness: 150 width: 300
He, et al. [6]	water	liquid cooled copper block configuration: 2	15 W/cm^2	~1 - 7 K/W	40x40x1.3	100	micro-pillars	d: 4.6-9.2 thickness: 17.7
Launay, et al. [7]	methanol	liquid cooled copper block configuration: 1	2 W/cm^2	900 W/m-K 0.8 K/W	20x20x1.05	172	triangular channels with liquid artery	width: 500 thickness: 342
Ivanova, et al. [8]	water	liquid cooled copper plate configuration: 3	70 W/cm^2	0.9 K/W	50x50x1	470	radial micro-capillary grooves	width: 80 – 400 thickness: 100

Table 1. continued

Author	Working fluid	Heat Sink and configuration	Heat flux/ heat input	Thermal resistance/ effective thermal conductivity	Dimensions, mm	Vapor core thickness, µm	Wick structure	Wick size, µm
Taniguchi, et al. [3]	water	fan cooled pin fin heat sink configuration: 4	-	4.79 - 8.89 K/W	33x33x0.4	100	micro-pillars	d: 30 thickness: 30

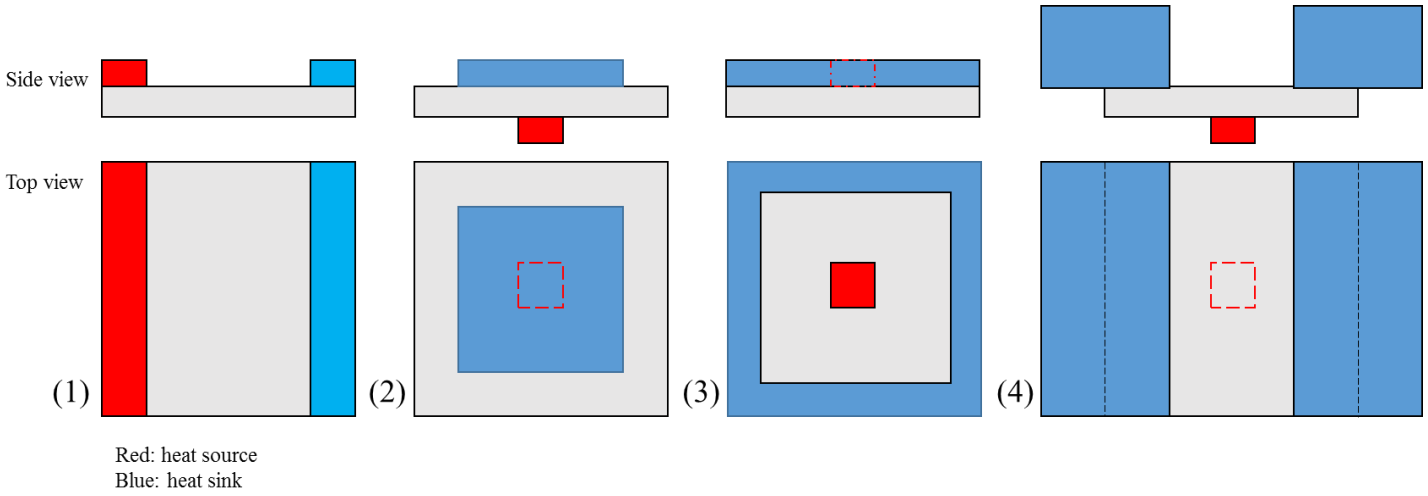

Figure 4. Heating and cooling configuration 1, 2, 3, and 4, for Table 1

Many numerical, analytical and computational models have been developed to study heat pipes and vapor chambers. Khrustalev and Faghri [9] presented a mathematical model for low-temperature axially grooved heat pipes, where fluid circulation, along with the heat and mass transfer processes during the evaporation and condensation were considered. Prasher [10] introduced a simplified conduction based modeling scheme to predict the heat transport capability of heat pipes and vapor chambers for various configurations, and derived an analytical model that studied the effective thermal conductivity of vapor. A three-dimensional model was developed by Vadakkan, et al. [11] to predict the performance of flat heat pipes in transient and steady-state with multiple discrete heat sources, through computation fluid dynamics based approach in the wick and vapor core, and heat conduction in the wall. Results showed that the axial diffusion through the wall and wick played an important role in determining the temperature distribution along flat heat pipes.

A steady-state, three-dimensional model was introduced by Xiao and Faghri [12] to analyze the thermal and flow behaviors of flat heat pipes. They included the heat conduction in the wall, fluid flow in the vapor chamber and porous wicks, and the coupled heat and mass transfer at the liquid/vapor interface. A transient, three-dimensional model for thermal transport in heat pipes and vapor chambers was developed by numerically solving a coupled wick-level micro and device-level macro model that accounted for the fluid flows in the wick structure and vapor core, and conduction in the wall, in order to determine the evaporation rate at the liquid-vapor interface and to predict the performance of a heat pipe [13].

1.3 Integration of Vapor Chamber into Interposer

Integration of vapor chamber into interposer is a possible solution for the thermal management of future portable electronics. As shown in Figure 5, a vapor chamber of submillimeter thick can be created inside the interposer. The vertical posts in the chamber serve as supporting structures for the vapor chamber under vacuum conditions, and serve as the structures for routing TSVs at the same time. Redistribution layers of fine and coarse pitches are implemented in the top and bottom side of the interposer, respectively. The peripheral extension of the interposer provides a condensation region to reject heat to the ambient. By utilizing the latent heat of liquid/vapor phase change of a working fluid, and capillary driven circulation of the working fluid in the vapor chamber, heat from two or three-dimensionally packaged devices can be spread evenly on the interposer, preventing the formation of hot spots.

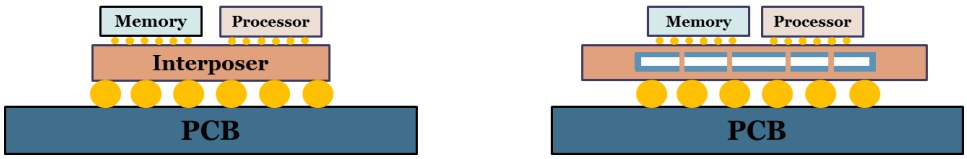

Figure 5. Integration of vapor chamber into interposer: (a) traditional interposer architecture; (b) proposed interposer with vapor chamber integrated architecture

1.4 The Present Work

The present work includes the following aspects:

1. Investigation of capillary pressure of different homogeneous wicks using Surface Evolver, fabrication process of 720 ±10 µm thick vapor chambers with patterned bi-porous monolayer copper powder wick structures.
2. Development of a charging station that evacuates and charges a vapor chamber at a rate of 10 µl/min.
3. Thermal characterization experiments for the fabricated vapor chambers to evaluate their performance.
4. Validation of the experimental results by a three-dimensional heat conduction model, coupled with a thermal resistance network for the vapor chamber.

Results from the experiments and models, and recommended future work are presented and discussed finally.

CHAPTER 2. VAPOR CHAMBER DESIGN AND MODEL

2.1 Introduction

In this chapter, fundamentals of heat pipe and vapor chamber are first reviewed. The capillary pressure head of different homogeneous wicks are next analyzed using the software Surface Evolver. Parametric studies of the capillary pressure, permeability, and effective thermal conductivity of wicks are discussed.

2.2 Heat Pipe Fundamentals

A heat pipe operates when the available net capillary pressure head is greater than the total pressure drop across the working fluid flow path. The condition where the capillary head balances the pressure drops is known as the capillary limit, and exceeding the heat input beyond this, results in dryout, where the continuous circulation of the working fluid is impeded. The net capillary pressure head results from the different radii of curvature of liquid-vapor interface at the evaporator and condenser. The total pressure drop within the working fluid flow path consists of the viscous drop when the condensed liquid transports through the wick structure from the condenser to evaporator, the viscous drop due to vapor transport through the vapor core from the evaporator to condenser, and the gravitational force encountered by the working liquid due to the orientation of the heat pipe. In order for the working fluid to maintain its circulation, the following condition must be met, known as the capillary limit:

$$\Delta P_c \geq \Delta P_l + \Delta P_v + \Delta P_g \tag{1}$$

2.2.1 Capillary pressure

Capillary pressure is defined as the pressure difference across a vapor/liquid interface and is governed by the Young-Laplace equation,

$$\Delta P_c = \frac{2\sigma}{r_{eff}} \tag{2}$$

where r_{eff} is the effective capillary radius, and σ is the surface tension of the liquid. The effective capillary radius of a wick structure depends on the size and porosity of a wick structure, and the contact angle between the interface and wick structure. A small contact angle means a good wettability between the liquid and wick structure. A small wick structure at a low porosity generates a small effective capillary radius. Thus, a wick structure with a good wettability, small size, and low porosity, creates a higher capillary pressure than the one with a poor wettability, larger size, and higher porosity. Figure 6 illustrates the liquid-vapor interface on a cylindrical array wick structure under capillary action,

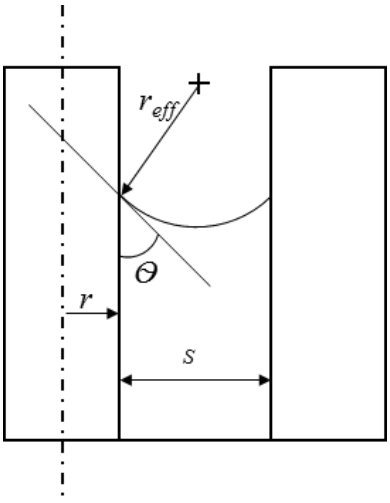

Figure 6. Meniscus on a cylindrical array wick structure

where r_{eff} is the effective capillary radius, r is the radius of the cylinderical wick, S is the spacing, and θ is the contact angle. The expressions of the effective capillary radius for several types of wick structure are available in Chi [14].

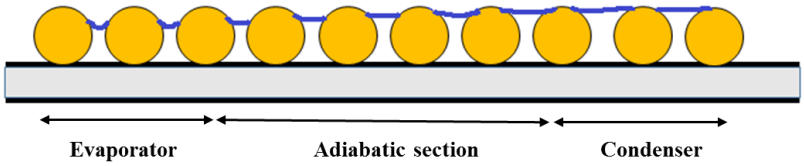

Figure 7. Liquid meniscus curvature along a heat pipe

Based on the Young-Laplace equation, the net capillary pressure head in a heat pipe across the evaporation and condensation regions can be expressed as:

$$\Delta P_c = \Delta P_{evap} - \Delta P_{cond} = \frac{2\gamma}{r_{evap}} - \frac{2\gamma}{r_{cond}} \tag{3}$$

where σ is the surface tension of a liquid, r_{evap} and r_{cond} are the effective capillary radii of a wick at the evaporator and condenser respectively, and ΔP_{evap} and ΔP_{cond} are the capillary pressure heads at the evaporator and condenser respectively. As shown in Figure 7, liquid at the evaporator tends to recede into the pores of the wick, and creates a curved meniscus that maintains a small contact angle. Hence, the effective capillary radius of the wick is very small at the evaporator. At the condenser, the effective capillary radius of the wick tends to be infinite due to the nearly flat meniscus, which is caused by the condensed liquid that is added into the wick to make it fully saturated or even flooded under some conditions. Therefore, the difference in capillary pressure heads between the evaporator and condenser creates a pressure gradient, that drives the working liquid to overcome different pressure drops during the transportation of the liquid from the condensation to

evaporation area. Under this condition, ΔP_c nearly equals ΔP_{evap}, which is the maximum value of ΔP_c.

$$\Delta P_{c,max} = \frac{2\gamma}{r_{evap}} = \frac{2\gamma}{r_{eff}} \tag{4}$$

2.2.2 Vapor pressure drop

The vapor pressure drop can be obtained by integrating the vapor pressure gradient in the direction of the vapor flow along a heat pipe by assuming that the flow is steady-state and one-dimensional, and is evaluated by Chi [14] as:

$$\Delta P_v = \left(\frac{C(f_v Re_v)\mu_v}{2\left(r_{h_v}\right)^2 A_v \rho_v h_{fg}} \right) L_{eff} q \tag{5}$$

where $L_{eff} = 0.5L_{evap} + L_{adia} + 0.5L_{cond}$

$$Re_v = \frac{2r_{h_v} q}{A_v \mu_v h_{fg}} \tag{6}$$

$$M_v = \frac{q}{A_v \rho_v h_{fg} \sqrt{\gamma_v R_v T_v}} \tag{7}$$

where r_{h_v} is the hydraulic radius of vapor core, C is a Mach number dependent constant, A_v is the vapor core cross-sectional area, f_v is the vapor flow friction factor, Re_v is the vapor flow Reynolds number, μ_v is the vapor dynamic viscosity, ρ_v is the vapor density, h_{fg} is the latent heat of vaporization, L_{eff} is the effective length of heat pipe, L_{evap} is the length of evaporation section, L_{adia} is the length of adiabatic section, L_{cond} is the length of condensation section, q is the heat input, M_v is the vapor flow Mach number, γ_v is the vapor specific heat ratio, R_v is the vapor gas constant, and T_v is the vapor temperature.

By calculating the vapor flow Reynolds number and Mach number, the condition of the vapor flow, whether it is laminar or turbulent, incompressible or compressible can be predicted, and the vapor flow friction factor can be calculated to determine the vapor pressure drop.

2.2.3 Liquid pressure drop

The liquid pressure drop can be obtained by integrating the liquid pressure gradient in the direction of the liquid flow along a heat pipe assuming that the flow is steady-state, laminar and one-dimensional, and is evaluated by Chi [14] as:

$$\Delta P_l = \left(\frac{\mu_l}{K A_{wick} \rho_l h_{fg}} \right) L_{eff} q \tag{8}$$

where μ_l is the liquid dynamic viscosity, ρ_l is the liquid density, h_{fg} is the latent heat of vaporization, A_{wick} is the cross-sectional area of wick structure, K is the permeability of wick structure, and L_{eff} is the effective length of heat pipe, and q is the heat input.

Permeability is an ability of a porous media that measures how well the media allows fluids to pass through it, and the permeability of a porous media is usually evaluated from experimental measurements that obey the Darcy's law. It is one of the important properties of a wick structure, and the permeability expressions for several types of wick structures are available in Chi [14].

2.2.4 Gravitational force

The gravitational force acting on the working liquid in a heat pipe consists of two components: the axial hydrostatic and normal hydrostatic pressure drop. The axial hydrostatic pressure drop is the component of the gravitational force acting along the

longitudinal axis, and the normal hydrostatic pressure drop is the component of the gravitational force acting perpendicular to the longitudinal axis of the heat pipe.

Axial hydrostatic pressure drop:

$$\Delta P_{||} = \rho_l g L \sin\psi \tag{9}$$

Normal hydrostatic pressure drop:

$$\Delta P_{\perp} = \rho_l g d_v \cos\psi \tag{10}$$

where ρ_l is the liquid density, g is the gravitation acceleration, L is the length of heat pipe, d_v is the diameter of vapor core, and ψ is the inclination angle of heat pipe.

2.3 Wick Structure and Review

Wick structures are porous media that allow fluids to permeate through under capillary action, which make them a key component in heat pipes and vapor chambers. A desirable wick structure will create a high capillary pressure or a small effective capillary radius, a good permeability to allow fluids to permeate through easily at reduced liquid pressure drop, and a high thermal conductivity, or a small thermal resistance. Wick structures used in commercial heat pipes include screen mesh, sintered metal powder, pillar array, microgroove or microchannel, and composite structure, which combine two or more wick structures to achieve a high capillary pressure, high permeability, and high thermal conductivity. Many studies on the performance of different kinds of wick structures for various heat pipes and vapor chambers were conducted in recent years. A detailed summary of the recent wick structure investigations is presented in Table 2.

Table 2. Recent studies of wick structures

Sintered Powder					
Author	**Working liquid**	**Performance**	**Wick structure**	**Figures**	**Dimensions**
Weibel, et al. [15]	water	q'': 500 - 596.5 W/cm^2 R_{wick}: 0.13 – 0.26 K/W ΔP_c: 11,430 Pa	mono-porous sintered copper powder		particle d: 45 – 355 µm thickness: 600 – 1200 µm porosity: 0.635 – 0.657
Chen, et al. [16]	water	q: 50 -360 W R_{VC}: 0.07 – 0.12 K/W	sintered copper powder mixed with diamond		copper: 80 – 325 mesh diamond: 80 – 170 mesh volume ratio of diamond: 1:8 – 1:4 thickness: 600 µm porosity: 0.5
Semenic and Catton [17]	water	q'': 232 – 990 W/cm^2 R_{wick}: 0.095 – 0.195 K/W-cm^2 ΔP_c: 11,571 – 16,299 Pa K: 3.00e-13 – 2.40e-12 m^2 k_{wick}: 4 – 22 W/m-k $k_{cluster}$: 132 – 147 W/m-k	bi-porous sintered copper powder	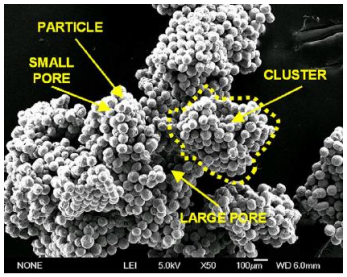	particle d: 41 – 63 µm cluster d: 302 – 892 µm thickness: 800 – 3000 µm particle porosity: 0.51 – 0.68 cluster porosity: 0.27 – 0.36
Zhao and Chen [18]	water	q'': 350 W/cm^2 r_{eff}: 13 µm	sintered copper powder with microgrooves	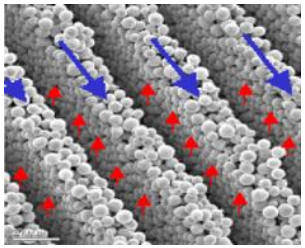	groove width: 150 – 500 µm bank width: 250 – 500 µm particle d: 50 µm thickness: 2000 µm

Table 2. continued

Author	Working liquid	Performance	Wick structure	Figures	Dimensions
Hwang, et al. [19]	water	q'': 387 W/cm^2 R_{evap}: 0.05 K/W-cm^2 r_{eff}: 30 µm K: 4.68e-12 m^2	monolayer sintered copper powder with liquid artery	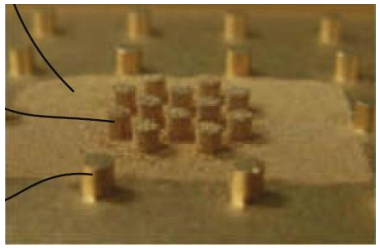	wick particle d: 60 µm artery particle d: 150 µm thickness: 60 µm porosity: 0.5
Hwang, et al. [20]	water	q'': 580 W/cm^2 R_{evap}: 0.055 K/W-cm^2	monolayer sintered copper powder with converging lateral arteries	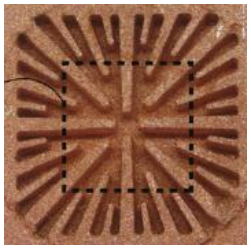	wick particle d: 60 µm artery particle d: 100 µm thickness: 60 µm porosity: 0.52
Sun, et al. [21]	water	q'': 220 W/cm^2 $R_{VC,hr}$: 0.0163 – 0.0260 K/W $k_{eff,VC}$: 6992.1 – 27489 W/m-K	sintered micro/nano structured copper powder with super-hydrophobic condenser side	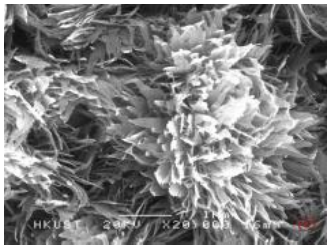	particle d: 57, 100 µm thickness: 500 µm
Weibel, et al. [22]	water	q'': 437 W/cm^2 r_{eff}: 21 µm K: 4.1e-11 m^2	sintered copper powder coated with CNT	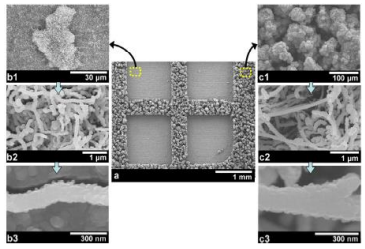	particle wick d: 100 µm CNT d: ~ 100 nm porosity: 0.5 thickness: 200 µm

Table 2. continued

Screen Mesh					
Author	**Working liquid**	**Performance**	**Wick Structure**	**Figures**	**Dimensions**
Yang, et al. [23]	water	R_{HP}: 3.54 K/W	copper screen mesh		wire d: 50, 115 µm thickness: 50, 115 µm
Li, et al. [24]	water	q'': 367.9 W/cm^2 $h_{eff,evap}$: 245.5 kW/m^2-K	sintered copper isotropic screen mesh	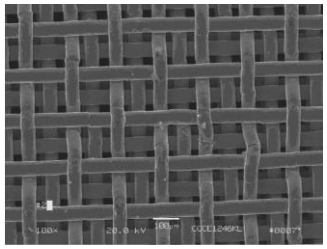	wire d: 56 µm thickness: 210 – 820 µm porosity: 0.693 - 737
Weibel, et al. [25]	water	q'': ~ 480 - 552 W/cm^2 R_{wick}: ~ 0.26 – 0.4 K/W	sintered copper screen mesh coated with CNT and copper	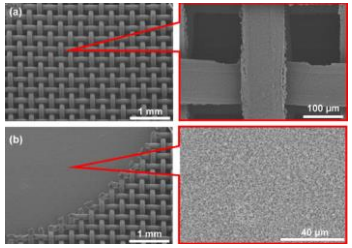	wire d: 104 µm wire spacing: 149 µm copper coating thickness: 500, 750 nm CNT number density: 5.2e7 – 2.5e8 #/cm^2
Foam					
Author	**Working liquid**	**Performance**	**Wick Structure**	**Figures**	**Dimensions**
Zhang, et al. [26]	water	Capillary pressure head: 80 – 113 mm	multiscale porous copper foam	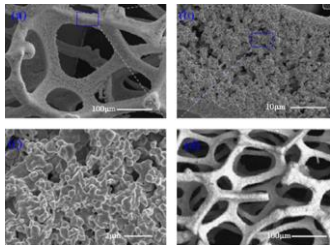	pore: 5 – 20 µm, 300 µm thickness: 1 – 2 mm

Table 2. continued

Pillar					
Author	**Working liquid**	**Performance**	**Wick Structure**	**Figures**	**Dimensions**
Taniguchi, et al. [3]	ethanol	R_{VC}: ~ 4.79 – 8.89 K/W	silicon pillar array	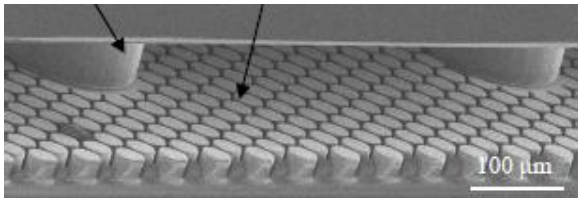	pillar d: 30 µm pillar pitch: 35 µm thickness: 30 µm
Ding, et al. [27]	water	$k_{eff,\ HP}$: ~ 130 - 350 W/m-K capillary velocity: ~ 27.5 mm/s at 2 mm – 5.5 mm/s at 10 mm	Ti pillar coated with nanostructured titania	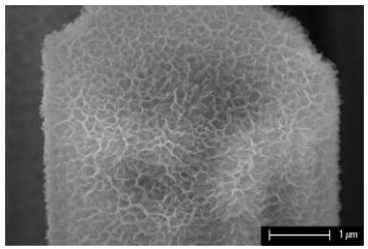	pillar d: 5 µm pillar pitch: 10 µm thickness: 50 µm nanostructured titania: ~ 200 nm
Nam, et al. [28]	water	q'' > 500 W/cm^2 $h_{eff,wick}$ > 10 W/cm^2-K	nanostructured Cu micropost	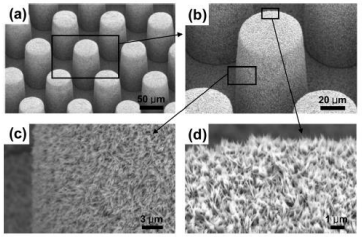	d: 50 µm pitch: 70 – 100 µm thickness: 100 µm porosity: 0.537 – 0.773
Ćoso, et al. [29]	water	q'': 119.6 - 733.1 W/cm^2 $h_{eff,wick}$: 19.6 - 20.7 W/cm^2-K	bi-porous wick with silicon pin-fins and microchannels	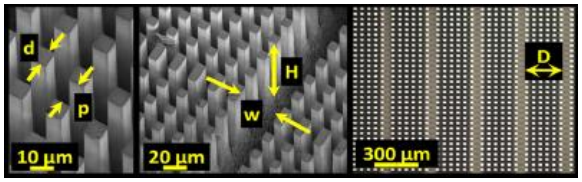	pin fin d: 3.1 – 29 µm pin fin spacing: 4.9 – 28 µm thickness: 56 – 243 µm array width: 144 – 288 µm microchannel width: 30 – 61 µm

Table 2. continued

Author	Working liquid	Performance	Wick Structure	Figures	Dimensions
Sharratt, et al. [30]	water	$q'' < 20$ W/cm^2 $h_{eff,wick}$: ~ 7 – 12.5 W/cm^2-K	Si/Cu nanostructured micro post in cylinder, pie and cluster shape	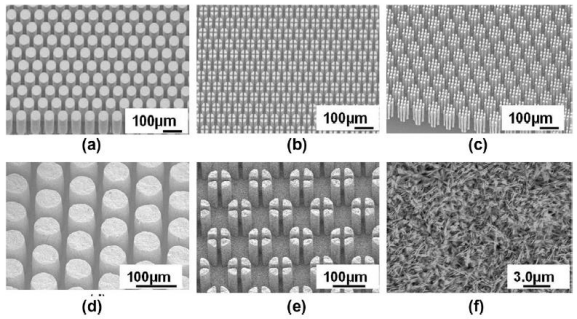	Si pillar d: 55 μm Si pillar pitch: 75 μm Si pillar height: 140 μm Cu pillar d: 75 μm Cu pillar pitch: 105, 124 μm Cu pillar height: 100 μm
Microgroove					
Author	**Working liquid**	**Performance**	**Wick Structure**	**Figures**	**Dimensions**
Yang, et al. [2]	water	R_{HP}: ~1.5 – 5.8 K/W	silicon microchannel with pin fin array supports	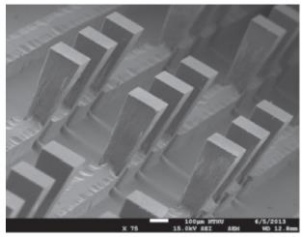	width: 200 μm spacing: 300 μm depth: 150 μm pin fin width: 200 μm pin fin height: 450 μm pin fin porosity: 0.923, 0.954
Chen, et al. [31]	acetone	q: 80 W R_{VP}: 0.72 – 1.04 K/W	aluminum radial grooved wick	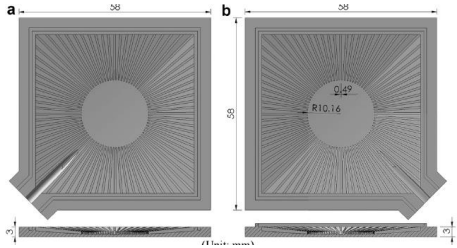	groove width: 400 μm groove depth: 910 – 1650 μm

Table 2. continued

Author	Working liquid	Performance	Wick Structure	Figures	Dimensions
Go [32]	acetone	R_{VP}: 0.45 – 0.76 K/W q'': 35 – 80 W/cm^2	metal-etched (stainless steel) microwick plate	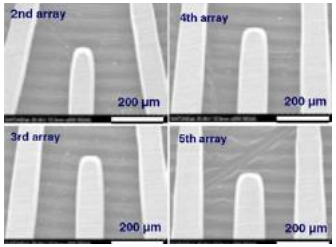	channel width: 100 µm channel spacing: 150 µm channel thickness: 110 µm
Peng, et al. [33]	water, ethanol	R_{VP} < 0.3 K/W $q \leq$ 90 W	leaf vein system grooved wick		channel height: 160 – 240 µm 1st channel length: 15 mm 1st channel width: 0.5 mm length ratio: 0.7
Carbon Nanotube					
Author	**Working liquid**	**Performance**	**Wick Structure**	**Figures**	**Dimensions**
Cai and Chen [34]	water	q'': 600 W/cm^2 $h_{eff,wick}$: ~ 22 W/m^2-K	CNT bi-wick with strip clusters	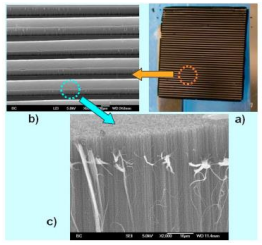	CNT d: < 20 nm cluster width: 100 µm cluster spacing: 50 µm cluster height: 250 µm

Table 2. continued

Author	Working liquid	Performance	Wick Structure	Figures	Dimensions
Cai and Bhunia [35]	water	q'': 770 W/cm^2 $h_{eff,wick}$: ~ 22.5 W/m^2-K	CNT bi-wick with pillar forests	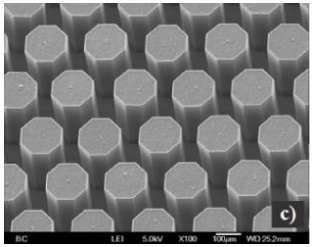	pillar d: 100 µm pillar spacing: 50 µm pillar height: 250 µm porosity: 0.95

2.4 Wick Structure Modeling

The previous section discusses common wick structures, such as screen mesh, sintered metal powder, pillar array, microgroove or microchannel, and other composite structures. Here, free liquid surfaces on four different homogenous wick structures, cylindrical pillar and spherical powder wick, in a hexagonal and square array, are modeled using the software Surface Evolver, to estimate the capillary pressure at different porosities. Results are compared to the existing data from Ranjan, et al. [36] for validation of the models. Next, the effects of porosity on capillary pressure, permeability and effective thermal conductivity of a wick structure are discussed. More details about the Surface Evolver and the modeling approach are presented in [37] and [36] respectively. The capillary pressure is normalized by the following equation:

$$\Delta P_{nor} = \frac{2\gamma}{r_{eff}}\frac{r}{\gamma} = \frac{2r}{r_{eff}} = \frac{2d}{d_{eff}} \tag{11}$$

where r and d are the radius and diameter of the sphere and cylinder wick respectively. Porosity is defined as the ratio of the void volume to the total volume of a wick structure. Porosity also defines the center to center distance, or the pitch between two unit-wicks. The geometrical parameters of the four homogenous wick structures are presented in Figure 8 and Table 3.

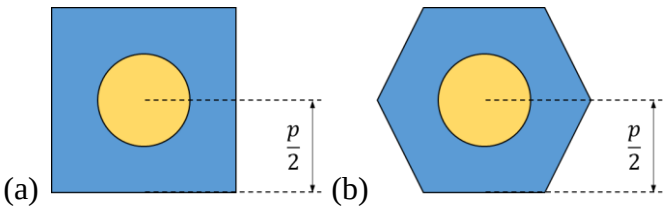

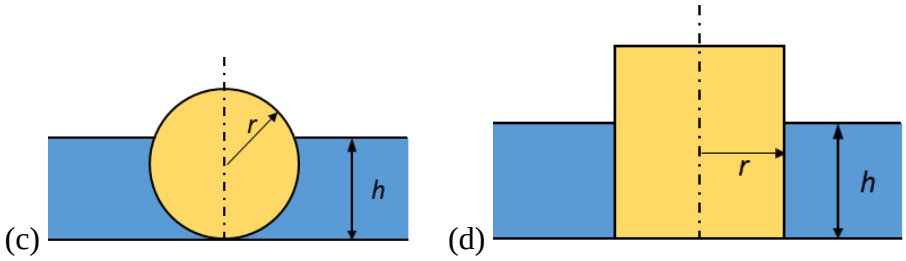

Figure 8. (a) Top view of spherical powder and cylindrical pillar in square array, (b) top view of spherical powder and cylindrical pillar in hexagonal array, (c) side view of spherical powder, (d) side view of the cylindrical pillar.

Table 3. Geometrical parameters of the four wick structures

Wick structure	Porosity, $\mathcal{E}$	Liquid volume, V/r^3
Cylindrical pillar, in square array	$1-\frac{\pi}{P^2}$	$H(P^2-\pi)$
Cylindrical pillar, in hexagonal array	$1-\frac{2\pi}{\sqrt{3}P^2}$	$H\left(\frac{\sqrt{3}}{2}P^2-\pi\right)$
Spherical powder, in square array	$1-\frac{2\pi}{3P^2}$	$HP^2-\frac{1}{3}\pi H^2(3-H)$
Spherical powder, in hexagonal array	$1-\frac{4\pi}{3\sqrt{3}P^2}$	$\frac{\sqrt{3}}{2}HP^2-\frac{1}{3}\pi H^2(3-H)$

where

$$P = \frac{p}{r}, \qquad H = \frac{h}{r} \tag{12}$$

Common wick structures usually have multiple layers, but the layer numbers of the modeled wick structures were set to 1. It was assumed that the layer number have a negligible effect on the capillary pressure [36]. Figure 9 shows the comparisons of the four wick structures along with the results from Ranjan, et al. [36] for validations.

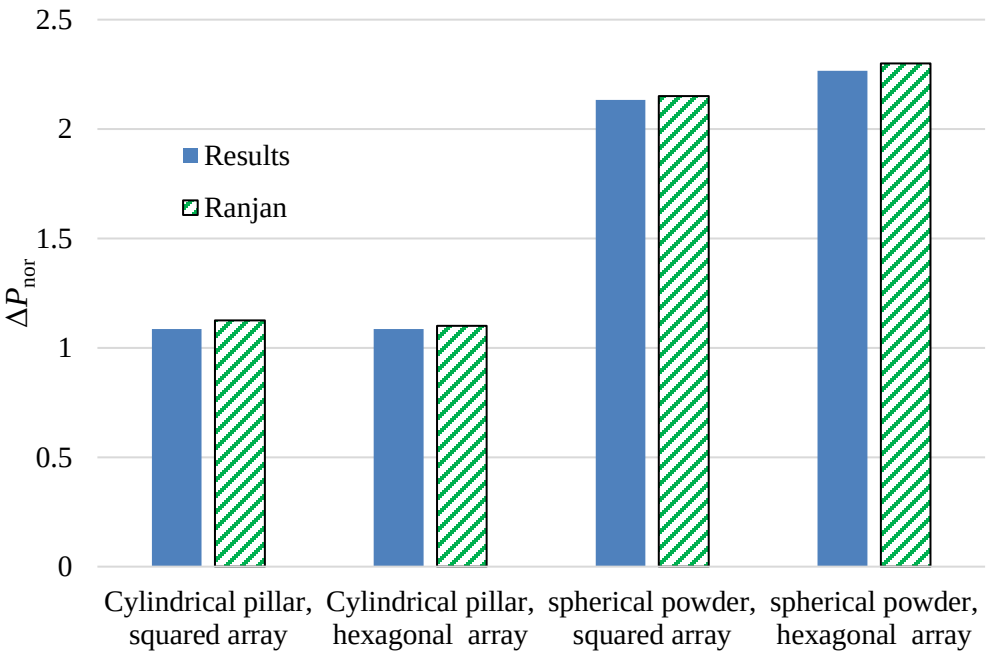

Figure 9. The maximum normalized capillary pressures of the four wick structures at a contact angle of 15 deg and a porosity of 0.64

Figure 9 shows that at a porosity of 0.64, the spherical powder wick structure in hexagonal array has the highest capillary pressure among the four wick structures. They all show good matchings to the results from Ranjan. Figure 10 shows that the spherical powder wick structure has higher capillary pressure than the cylindrical pillar wick structure at the

same porosity. Also, the spherical powder wick structure in hexagonal array has better thin-film evaporation area percentage than the other three wick structures [36], where the thin-film evaporation plays an important role in heat transfer in heat pipes and vapor chambers. mong the shapes considered, the spherical powder wick structure in hexagonal array has the best performance in terms of the capillary pressure, and thin-film evaporation among the four wick structures. Hence, it was chosen for designing the thin silicon vapor chamber.

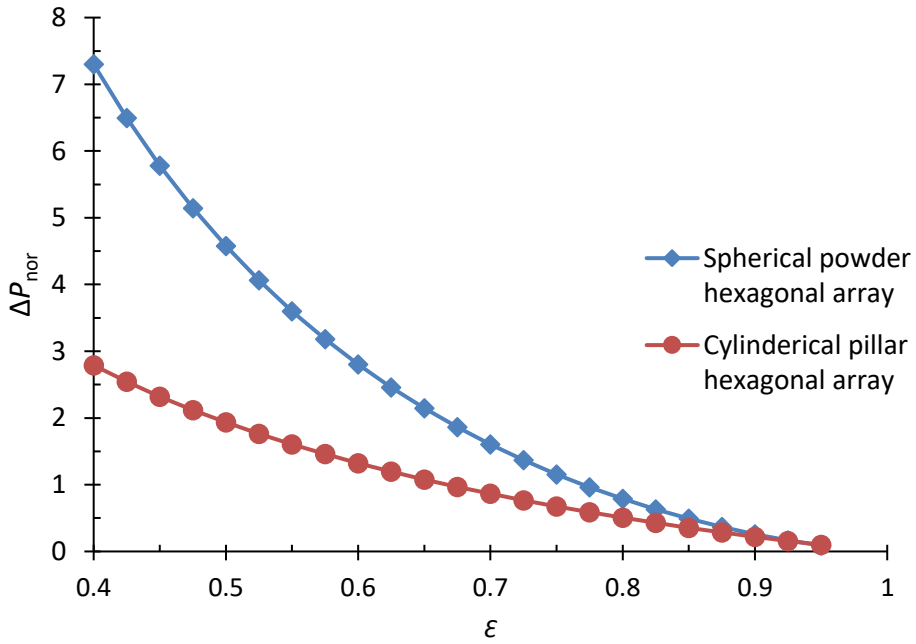

Figure 10. Comparison of the capillary pressures between the spherical powder and cylindrical pillar wick structure in hexagonal array at different porosities, at a contact angle of 10 deg, H = 0.8r and H = r respectively

For the spherical powder wick structure, the maximum capillary pressure varies with the liquid height and the pitch. For example, the optimal liquid height, height when the maximum capillary pressure is obtained, is about 0.8 of the radius, at a porosity of 0.64. A global maximum capillary pressure is obtained when the pitch and liquid height tend to be the sphere diameter and radius, respectively. As the pitch increases, the optimal liquid height decreases. More details are presented in [38]. Assume that the liquid height for the

spherical powder wick structure in hexagonal array is about 0.8 of the sphere radius [36], and the contact angle is chosen to be 10 deg for copper and water [39], a correlation between the maximum normalized capillary pressure and the porosity is given below.

$$\Delta P_{nor} = 6.7253 \frac{(1-\varepsilon)^{1.4576}}{\varepsilon^{0.9021}}, \text{ for } 0.395 \leq \varepsilon \leq 0.951, H = 0.8, CA = 10 \qquad (13)$$

Permeability and effective thermal conductivity are the other two important factors that significantly affect the performance of a wick. Permeability is a capability of a porous media that measures how well fluids can permeate through, and is related to the porosity of the media. If the porosity of a wick is high, the permeability of the wick is also high, and vice versa. However, a highly porous wick will have a small capillary pressure as mentioned before. Hence, a term that describes the heat transfer capability of a wick by balancing between capillary pressure and permeability, is called the capillary performance, K/r_{eff} or K/d_{eff}. Nam, et al. [40] presented a study to characterize the capillary performance of a superhydrophilic Cu micro-post array wick, and showed that its capillary performance increased with porosity. From Chi [14], an expression of the permeability for close packed sphere wicks is shown in Equation 14, and expressions of the permeability for several wicks are also available.

$$K = \frac{\varepsilon^3}{150(1-\varepsilon)^2} d^2 \qquad (14)$$

Equation 15 [41] estimates the effective thermal conductivity of a wick, based on its porosity, and the thermal conductivities of a liquid and solid phase material.

$$k_w = \frac{k_l[(2k_l + k_s) - 2(1-\varepsilon)(k_l - k_s)]}{[(2k_l + k_s) + (1-\varepsilon)(k_l - k_s)]} \qquad (15)$$

where k_w is the effective thermal conductivity of a wick, k_l and k_s are the thermal conductivities of a liquid and a solid respectively. By computing the K/d_{eff} of the spherical powder wick structure in hexagonal array using Equations 13 & 14, and the effective thermal conductivity using Equation 15 (water as the liquid and copper as the solid), a relationship between these two terms are shown in Figure 11 after normalization. It can be shown that there exists an optimal porosity near 0.75 that balances the capillary performance and effective thermal conductivity of the spherical powder wick structure. At this porosity, the wick structure is expected to exhibit a high permeability to let fluid flow through easily under a high capillary pressure, and remain a high effective thermal conductivity at the same time. This gave an idea for fabricating a vapor chamber that could operate under a high heat flux with a low thermal resistance, by finding an optimal porosity for the wick structure or optimal spacing between the wicks.

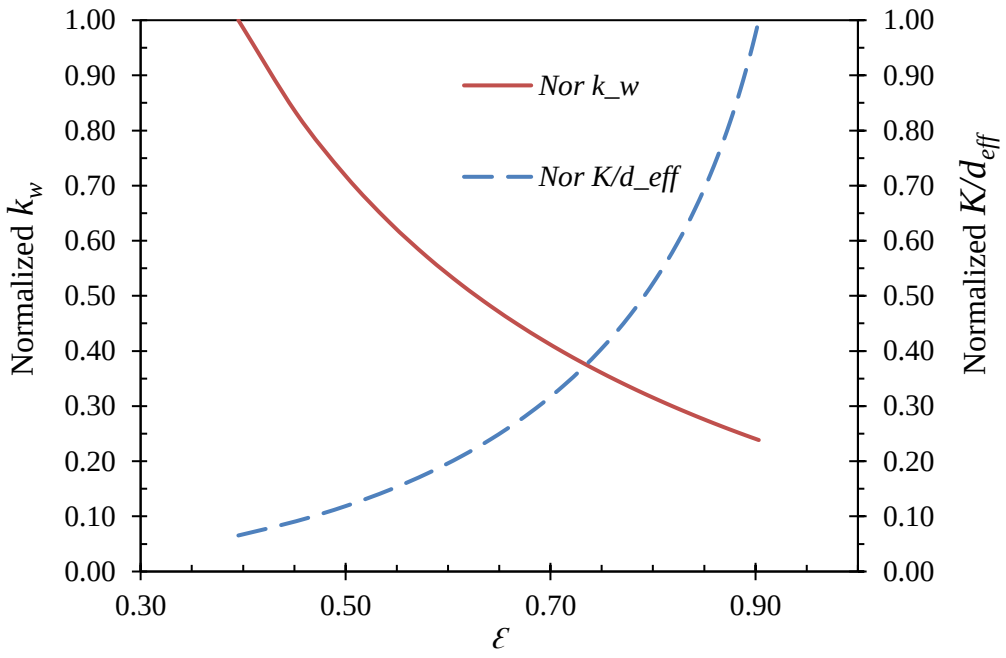

Figure 11. Normalized capillary performance and normalized effective thermal conductivity of the spherical powder wick structure in hexagonal array at different porosities

2.5 Working Fluid Selection

In order for a vapor chamber or heat pipe to operate properly, the capillary limit must be met, as described by Equation 1. In [42], a maximum heat transfer rate for a heat pipe can be obtained by solving Equation 1, assuming constant liquid properties and uniform wicks along the heat pipe, and insignificant pressure drop due to the vapor flow.

$$q_{max} = \left[\frac{\rho_l \sigma h_{fg}}{\mu_l}\right]\left[\frac{KA_{wick}}{L}\right]\left[\frac{2}{r_{eff}} - \frac{\rho_l g L}{\sigma}\sin\psi\right] \tag{16}$$

where ρ_l is the liquid density, σ is the liquid surface tension, h_{fg} is the latent heat of vaporization, μ_l is the liquid dynamic viscosity, K is the permeability of wick structure,

A_{wick} is the cross-sectional area of wick structure, L is the length of heat pipe, r_{eff} is the effective capillary radius, g is the gravity, and ψ is the inclination angle of heat pipe.

As shown in Equation 16, the maximum heat transfer rate depends on the properties of the working fluid, wick structure, and heat pipe. The term, known as the merit number M,

$$\frac{\rho_l \sigma h_{fg}}{\mu_l}$$

is defined only by the properties of the working fluid. It plays a significant role in selecting a working fluid for a vapor chamber or heat pipe, in order to achieve an optimized performance under an operating temperature range. As shown in [43], water has the highest merit number among many different working fluids, from 20 ^{o}C to 250 ^{o}C. Additionally, the effective thermal conductivity of water is much higher than that of many fluids [44], which can give a high effective thermal conductivity for a wick structure. Hence, water is a common working fluid in vapor chambers or heat pipes, and it was chosen for designing the thin silicon vapor chamber.

CHAPTER 3. FABRICATION AND EXPERIMENTS

In this chapter, details about the fabrication process of the vapor chambers with patterned bi-porous monolayer copper powder wick structures at different porosities are provided. The charging station that evacuates and charges the studied vapor chambers with a working liquid is discussed. Also, the test setup for thermal characterization of the vapor chamber is described.

3.1 Fabrication and Assembly of Vapor Chamber

The fabrication of the vapor chamber consists of processing the top and bottom wafers, followed by their bonding. A schematic of the process flow is shown in Figure 12. A 525 ±25 µm thick top wafer was first coated with 11 µm negative photoresist (Futurrex NR5 - 8000) by a spinner (BLE Spinner), then exposed for patterning by a mask aligner (Karl Suss TSA MA-6), and finally developed in a resist developer RD6. Detailed recipes about the photoresist coating can be found in www.futurrex.com. The undeveloped photoresist residuals left on the wafer were cleaned by a reactive ion etcher plasma system (Vision 320 RIE). 275 µm deep vias of 1.7 mm diameter were next etched on the front side by deep reactive ion etching (DRIE), followed by a deposition of 0.5 µm silicon oxide layer by plasma enhanced chemical vapor deposition (PECVD). The back side of the wafer was thinned by etching 325 µm to expose the etched vias. The wafer was diced into 30 mm x 30 mm pieces by a dicing saw (ADT 7100), which ultimately served as the top substrate for the vapor chamber.

Similarly, a 525±25 µm bottom wafer was first coated with 8 µm negative photoresist and then exposed for patterning. A 300 µm deep 20 mm x 20 mm chamber and 16 evenly spaced supporting posts with 1 mm diameter were created by etching, followed by a deposition of 0.5 µm silicon oxide layer. The wafer was diced into 30 mm x 30 mm

pieces serving as the bottom substrate of the vapor chamber. A 5 mm wide peripheral extension serving as the condenser was created to reject heat to the ambient.

In order to create the spherical powder wick structure on the silicon substrate, NOA 89 UV adhesive from Norland was patterned as dot arrays on the chamber's substrate by inkjet printing (MicroFab JetLab II Inkjet Printer, 50 μm ink-jet head). Adhesive dot arrays were printed at different spacings to achieve different wick porosities using programmed scripts. Copper powder with an average diameter of 85±3 μm was then deposited by pipette and self-assembled to the adhesive dots by capillary forces. A 5 min UV curing followed by a 40 min UV aging to the adhesives consolidated the powder on the substrate. Next, the substrate was flushed with DI water to wash away any powder not attached to the adhesive dots. The wafer was then dried using compressed nitrogen gas, and the patterned bi-porous monolayer copper powder wick structure on the silicon substrate, which consisted of many small dense powder wick clusters, was created. The porosity of the wick structure was calculated based on the weight of the final wick structure, over the weight of a solid copper occupying the volume of the entire wick structure layer. Figure 13 shows images of the inkjet printed adhesive dots and final wick structures at different porosities. As the figure shows, several copper particles were attached to an adhesive dot to form a local wick cluster, since the diameter of an adhesive dot was about 180 μm, which allows for the attachment of bi-porous monolayer copper powder during the self-assembly process.

To bond the top and bottom substrates of the vapor chamber, a thin film of low outgassing epoxy (3M Scotch-Weld Epoxy Potting Compound DP270 Clear) was spun on a bare silicon wafer. The film was then transferred to the top surface of the peripheral extension and the posts of the bottom substrate, followed by bonding to the top substrate under a constant pressure, and a temperature of 60 ^{o}C for 24 hrs. Two 1/16 inches ID copper tubes were attached to the vias for evacuation and charging using an epoxy (JB Kwikweld),

followed by 24 hrs of curing at 50 ^{o}C. Figure **15** and Table 4 show the dimensions of the vapor chamber.

Top wafer

1. DRIE for vias after photolithography

2. Oxidization

3. DRIE for etching through and thinning

Bottom wafer

1. DRIE for chamber after photolithography

2. Oxidization

3. Inkjet printing UV adhesive dots

4. Deposition of copper powder and UV curing

Bonding two substrates using epoxy and heat curing

Figure 12. The fabrication process of the vapor chamber

(1a) 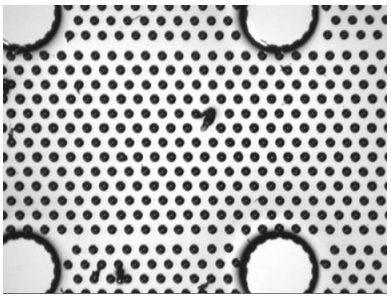 (1b) 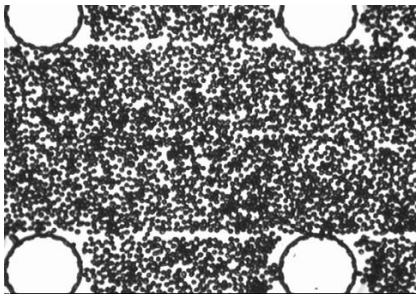

(2a) 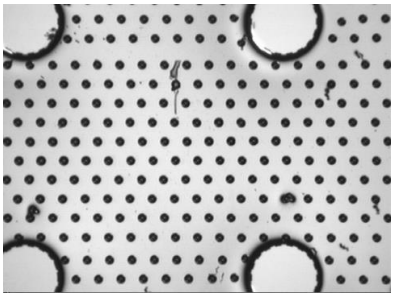 (2b) 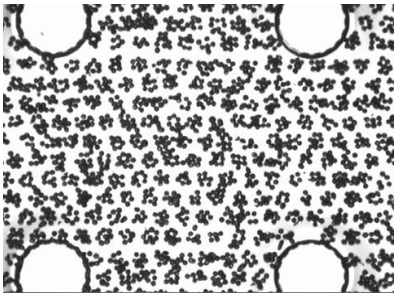

(3a) 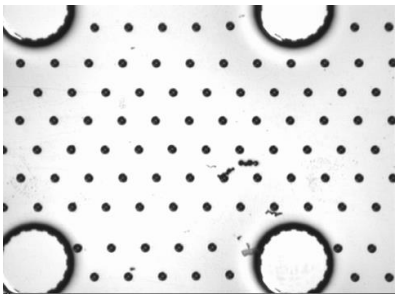 (3b) 

(4) 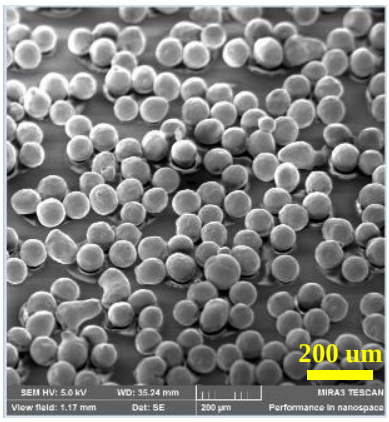

(5) 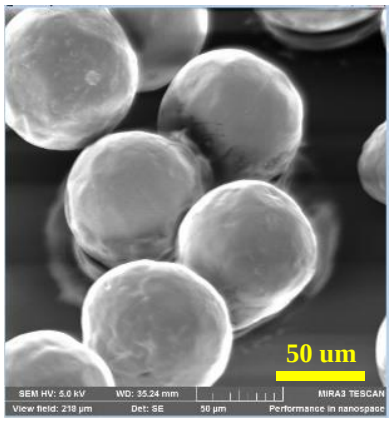

Figure 13. (1a) & (1b) adhesive dot arrays and wick at a porosity of 0.54 respectively; (2a) & (2b) adhesive dot arrays and wick at a porosity of 0.75 respectively; (3a) & (3b) adhesive dot arrays and wick at a porosity of 0.88 respectively; (4) & (5) SEM images of wick at a porosity of 0.66

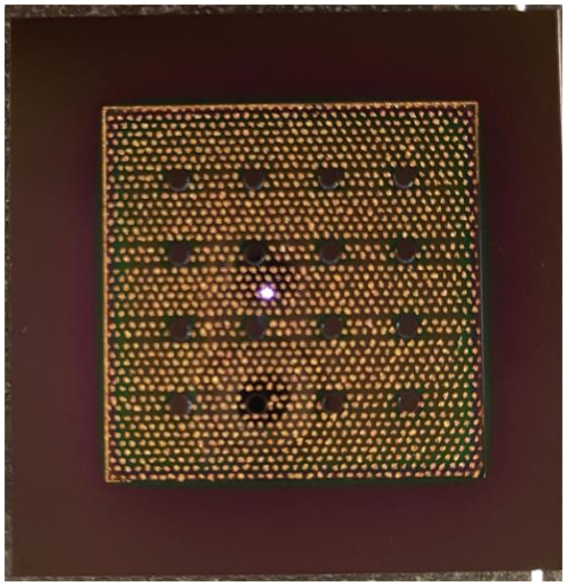

Figure 14. Top view of a bottom substrate with the wick structure at a porosity of 0.881

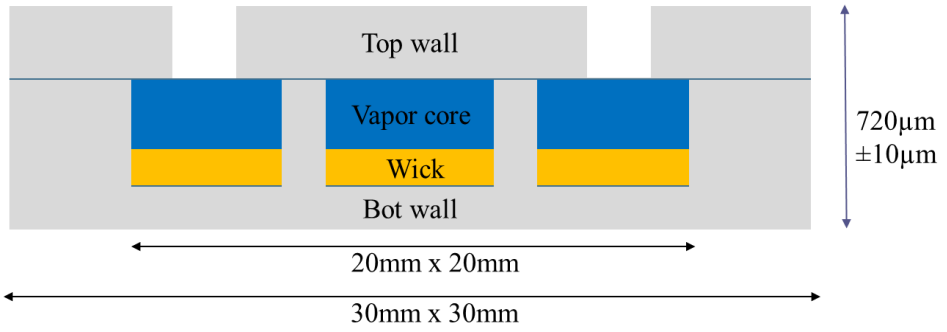

Figure 15**. Dimensions of the vapor chamber**

Table 4. Layer thicknesses of the vapor chamber

Layer	Thickness (µm)
Top wall	200
Vapor Core	215
Wick	85
Bot wall	225

3.2 Vapor Chamber Charging

To function, a vapor chamber requires a proper amount of a working fluid, charged under vacuum conditions, after removing any non-condensable gasses. The charging process for vapor chambers and heat pipes has been studied extensively [5, 45-47]. Figure 16 presents a schematic of the charging apparatus assembled for this study and Figure 17 shows the actual charging station. The charging station consists of a turbo vacuum pumping

station (Pfeiffer Vacuum HiCube 80 Eco) that can evacuate air to a vacuum level of 10^{-7} hPa, a rotary vacuum pump, a high current vacuum gauge (Pfeiffer Vacuum PKR 361) with a measurement range from 10^{-8} hPa to 10^{3} hPa, several vacuum valves and ball valves, a peristaltic pump system using a Tygon E-LFL tubing (Cole-Parmer Masterflex) that can deliver liquid at a rate of 1 µl/min, a flask and an ice bath, and tube connections. To evacuate the air inside the vapor chamber, firstly we turned on the turbo vacuum pump, then opened valve V1, while valves V2 and V3 were closed, and the peristaltic pump head was unfastened. Next, valve V2 was slowly opened to allow the air from valve V3 to valve V1 to be evacuated. When the vacuum level reached 1.2 Pa, the vacuum tube on the left was crimped and then cut. A vacuum gauge was installed close to the vapor chamber, in order to accurately measure the vacuum level of the vapor chamber. The rotary vacuum pump evacuated the air from valve V3 to valve V5, and degassed the liquid in the flask while valve V3 and valve V5 were closed, and valve V4 was opened. Next, the rotary vacuum pump was turned off and valve V5 was opened to allow the liquid to exit to valve V3. The de-ionized (DI) water serving as the working liquid was stored in the flask, which was immersed in ice water. To charge the vapor chamber with the working liquid, firstly the peristaltic pump head was fastened, then opened valve V3 and pumped the liquid at a rate of 30 µl/min (under the continuous mode) to the entrance of the charging tube. Next, we pumped a predetermined amount of liquid at a rate of 10 µl/min under the volume dispense mode. After that, the charging tube on the right was crimped and cut, and the vapor chamber was detached from the charging station. The amount of liquid charged was then determined from the weight difference of the vapor chamber before and after the charging, using a precision balance (Analytical Balance HR-100AZ) with an uncertainty

of ±0.1 mg. The calibration of the charging process was done by following the above procedure on 1/16" *ID* copper tubes, instead of vapor chambers, and the result is shown in Figure 18. **Figure 19** shows a vapor chamber with crimped and cut vacuum and charging tubes, after the charging process.

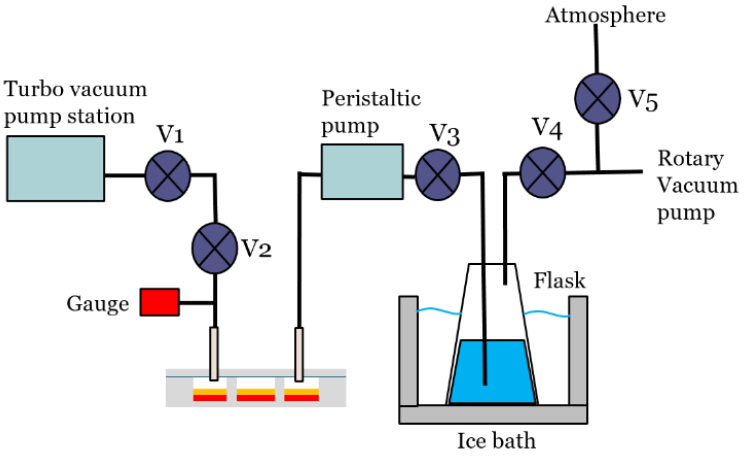

Figure 16. The schematic of the vapor chamber charging station

(a) 

(b) 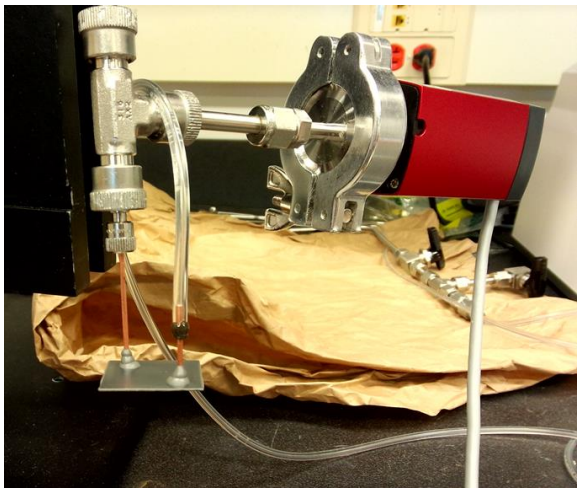

(c) 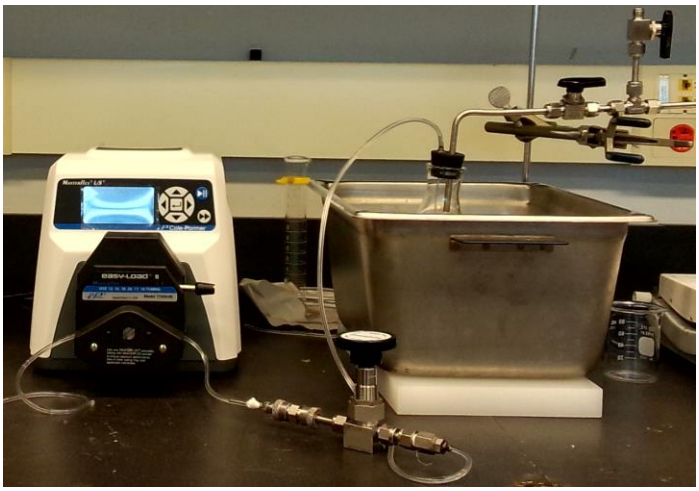

Figure 17. The charging station: (a) the turbo vacuum pumping station; (b) the vapor chamber connections and the vacuum gauge; (c) the peristaltic pump system and the flask connections

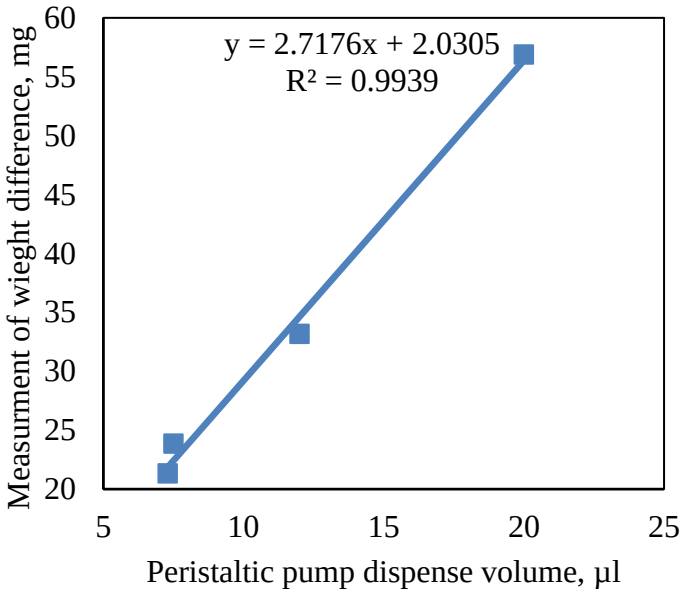

Figure 18. The calibration of the charging process

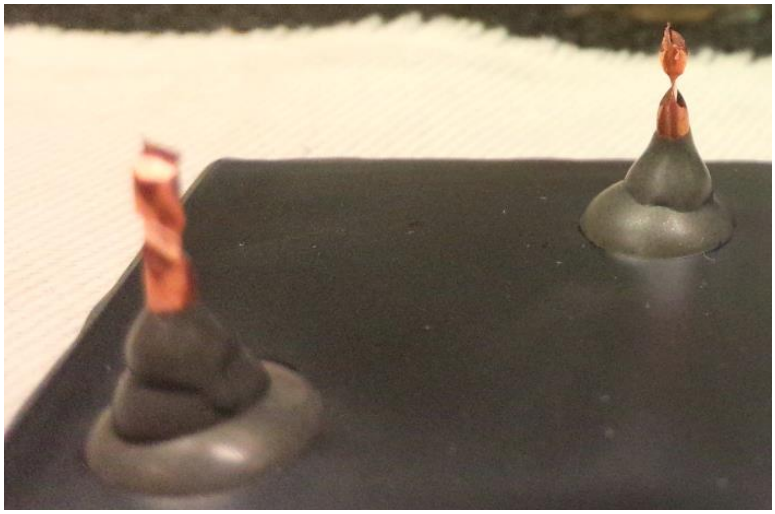

Figure 19. Crimped and cut vacuum and charging tubes

3.3 Thermal Characterization Experiments

The test setup is showed in Figure 20 and Figure 21. In Figure 20, an aluminum pin-fin heat sink with dimensions as shown was attached to the top surface of the vapor chamber by an 80 µm thick thermal interface material (TIM pad, AI Technology COOL-BOND PSA-3NC). As shown in Figure 20 (a), the center volume of the heat sink was removed, and the top 20 mm x 20 mm surface area of the vapor chamber was thermally insulated, which allowed to form a condensation region on the peripheral extension of the vapor chamber. A 1 mm thick, 5 mm x 2.5 mm, 50 Ω resistive heater (Barry Industries 20W AIN Leaded Resistor) was attached to the bottom center of the vapor chamber by a 240 µm thick TIM pad (AI Technology COOL-BOND PSA-3NC) to simulate a small die with a power input of up to 20W.

As shown in Figure 20, 4 thermocouples (OMEGA T-type L-0044T) of 0.25 mm diameter wire were attached to the middle of the edges of the 20 mm x 20 mm top surface of the vapor chamber to measure the condenser temperature. A 10 μm thick flat surface thermocouple (OMEGA T-type CO2-T) was inserted between the 240 μm TIM pad and the bottom surface to measure the evaporator temperature. Before testing, the charging and vacuum tubes, and the sidewalls of the vapor chamber were insulated using an epoxy. Glass wool was used to thermally insulate the 4 thermocouples, the entire 20 mm x 20 mm top surface, the side walls and the bottom surface of the vapor chamber, the side walls of the heater, and the base of the heat sink. The vapor chamber with the heater attached was seated on a piece of glass wool and an insulation foam block (FOAMULAR® 150), in order to minimize heat losses.

In Figure 21, a power supply (Agilent E3649A) connects to the heater and a fan (NMB 3612KL-04W-B66) to supply power, and a data acquisition unit (Agilent 34970A) collects data from the thermocouples and connects to a computer. A copper block was placed on the heat sink to apply a constant pressure and make the vapor chamber level during tests. The thermocouples were calibrated before testing using an ice bath and an OMEGA CL122 block calibrator, which simulated heating and cooling sources in one unit. During testing, room temperature was maintained at approximately 21 ± 0.5 ^{o}C, and the fan at a voltage of 14 V delivered ~22 CFM (at fan speed 1260 ± 10 RPM). At the beginning of testing, the fan blew air for 10 min to obtain a stabilized boundary condition, and then the voltage of the heater was increased at 1 V increments, every 20 min. After several increments, the power for the heater and fan was turned off, and the test was repeated in

20 hrs or more. The thermal resistance of the vapor chamber was calculated by the following equation,

$$R = \frac{T_{evap} - T_{cond,avg}}{q} \tag{17}$$

where T_{evap} is the temperature at the evaporator, $T_{cond,avg}$ is the average temperature at the condenser, and q is the power applied to the heater. Heat flux was computed based on the applied power and the cross-sectional area of the heater (5 mm by 2.5 mm).

There were three different tests conducted to evaluate the performance of the vapor chambers. Vapor chambers at porosities of approximately 0.78 under different wick saturation ratios were tested. The wick saturation ratio was defined as the charged liquid volume relative to the porous volume of the wick structure. Three vapor chambers at different porosities with a wick saturation ratio of approximately 54% were tested, and 120 hrs continuous tests were conducted to evaluate the samples' performance reliability. Table 5 summarizes the samples' parameters.

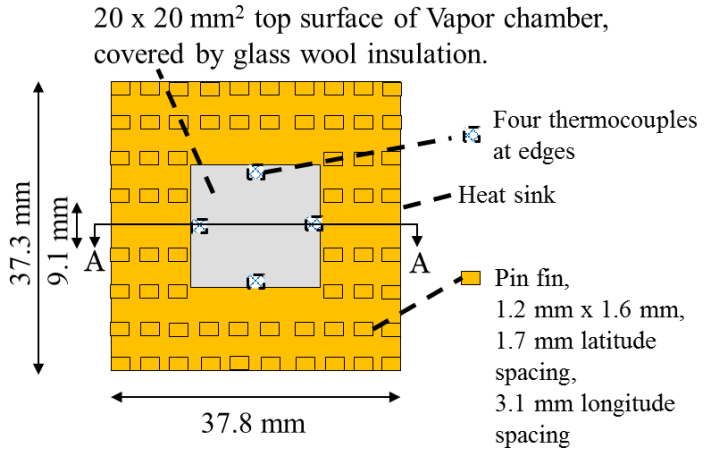

(a)

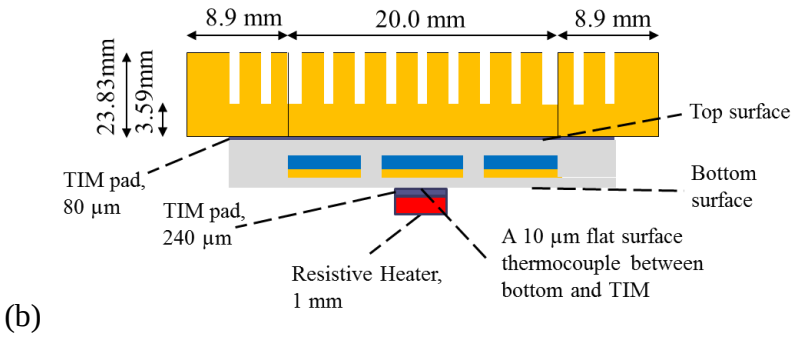

(b)

Figure 20. Temperature measurements and dimensions of the components: (a) top view, (b) A-A cross-section view

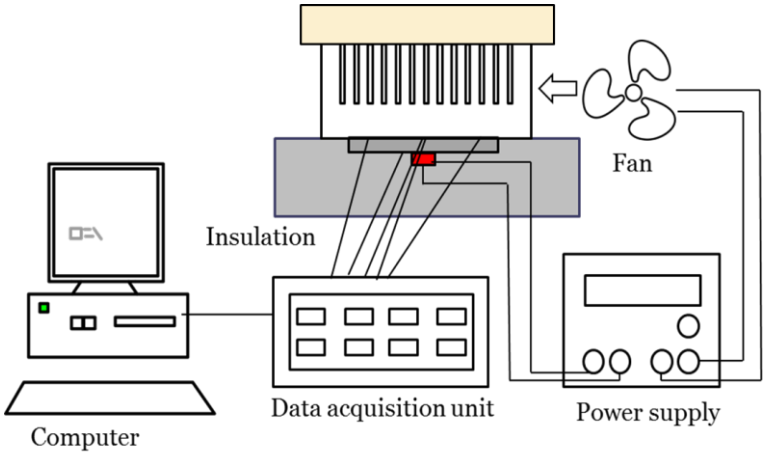

Figure 21. Equipment setup

Table 5. Sample parameters

#	Porosity, uncertainty ± 0.015	Wick Saturation Ratio (%)
1	0.546	53 ± 2
2	0.789	167 ± 6
3	0.798	85 ± 3
4	0.767	58 ± 2
5	0.897	50 ± 2
6	0.579	0

3.4 Uncertainty

The uncertainties in the measurements were estimated by considering both measurement variance and resolution. The size of the powder copper particle has an uncertainty of ±3 μm. The wick porosity has an uncertainty of ± 0.015. The largest uncertainty of the wick saturation ratio is ± 6%. Thermocouples were calibrated using an Omega CL122 calibrator and an ice bath to obtain an uncertainty of ± 0.05K. The voltage and the current were measured using a digital multimeter (Fluke 179) with uncertainties of ± 0.05% and ± 0.5%, respectively. The error bars in the figures of the next Chapter show the estimated uncertainties of the thermal resistance. Heat losses were estimated to be less

than 3.5%, by estimating heat leakage through conduction from the heater to the surrounding insulation materials.

CHAPTER 4. RESULTS AND DISCUSSION

In this chapter, experimental results of the vapor chambers with different wick saturation ratios and porosities, and their extended performance are presented. Also, a simplified three-dimensional heat conduction model, and a simplified one-dimensional thermal resistance network were developed to validate the experimental results.

4.1 Effect of Wick Saturation Ratio

Vapor chambers at porosities of approximately 0.78, under three different wick saturation ratios were tested, and the results are shown in Figure 22. Their performance was compared with an uncharged sample with a fluid cavity, and a 750 ± 25 μm thick, 30 mm x 30 mm solid silicon substrate. The uncharged sample was evacuated, and without any working liquid, so it could be assumed that conduction was the only heat transfer mode in the sample. Thermal resistance for this case was nearly constant, as shown in the figure. By comparing results of the charged and uncharged samples, the lowest thermal resistance of a charged sample was 38% of the uncharged sample. The charged liquid has a significant effect in decreasing the thermal resistance of the vapor chamber, since heat transfer is dominated by the phase change within the vapor chamber. Also, the lowest thermal resistance of a charged sample was about 74% of the solid silicon thermal resistance.

All samples showed decreased thermal resistance as the heat flux increased until they reached their minimum thermal resistance, after which the thermal resistance gradually increased with heat flux. The heat flux at the minimum thermal resistance corresponded to dryout, with degradation of performance at increased heat flux. Sample #3 showed the lowest thermal resistance of approximately 2.4 K/W at 5.6 W/cm^2, while the lowest thermal resistance of the oversaturated Sample #2 was approximately 4.1 K/W at 5.6 W/cm^2, which was almost 2x larger than that of Sample #3. Ranjan, et al. [36] found

that the wick saturation ratio affects the surface area for thin film evaporation, which plays a significant role in the heat transfer within a vapor chamber. As the wick saturation ratio changes, the thin film evaporation area, which is based on the liquid free surface area and the percentage of the thin film area, also changes. Sample #3 with 85% wick saturation ratio had the best balance between the liquid free surface area and the percentage of the thin film area, and thus the lowest thermal resistance. Oversaturation can restrict the thin film evaporation on the wick surface. The excessive liquid reduces the thickness, or the volume, of the vapor core for condensation. Hence, it leads to an increased vapor pressure drop and a downgraded performance. The results show similar trends for the samples, since their wick porosities were similar, but their values were significantly impacted by wick saturation ratios, as discussed above.

Sample #4 had the highest dryout heat flux of 7.6 W/cm^2, reflecting the effect of meniscus height and wick separation on the capillary pressure of the sphere wicks [38]. For a close packed monolayer sphere wick structure, the greatest capillary pressure is achieved when the meniscus height is close to the sphere radius, implying that wick saturation ratio near 50% gives the best capillary head. This wick saturation ratio was used for the other two vapor chambers, since it gave the highest dryout heat flux. The very large error bars at the lowest heat flux are due to the resolution uncertainties of the thermocouples at very small temperature differences.

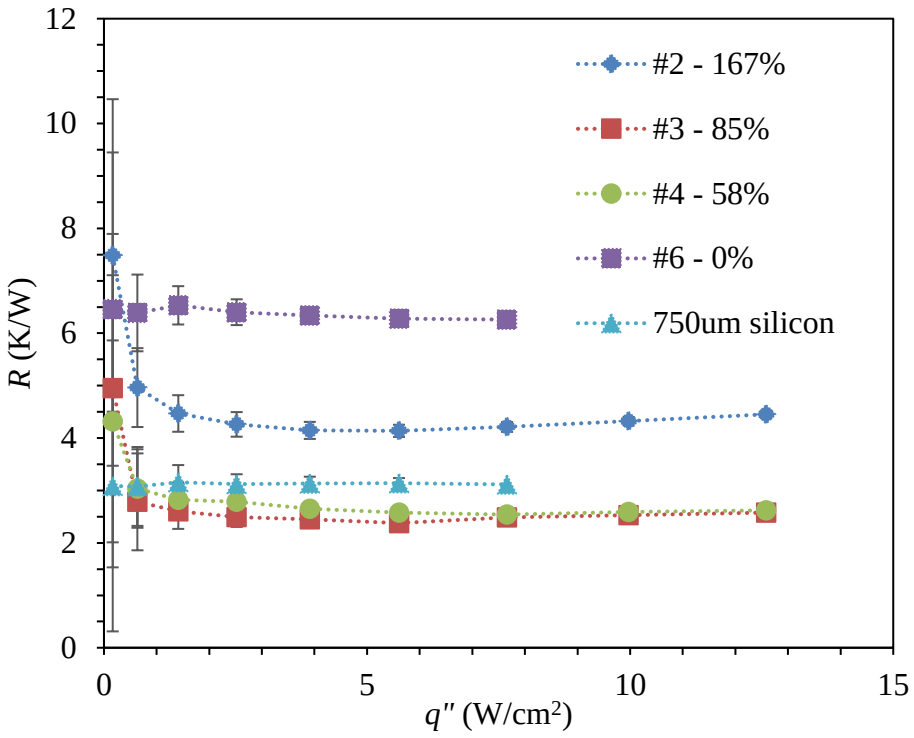

Figure 22. Thermal resistance of the samples at porosities of approximately 0.78 under three different wick saturation ratio.

4.2 Effect of Porosity

Vapor chambers at porosities of 0.546, 0.767, and 0.897 were tested, and compared to the solid silicon substrate. The results are shown in Figure 23. Sample #5, with the highest porosity, showed the highest thermal resistance due to the sparse wicks on the evaporator, resulting in reduced area for the thin film evaporation to take place. Sample #4 at a porosity of 0.767 had a less dense wick structure than Sample 1 but performed better. This is because it had a better balance between capillary pressure and permeability, which allowed the working fluid to flow and be supplied to the wicks more easily. The dense wick structure in sample #1 caused a low permeability for the liquid to be supplied to the wicks. This resulted in inadequate and uneven thin film evaporation, which lead to a reduced heat

transfer performance in Sample #1. All three samples reached their lowest thermal resistance at a heat flux of 7.6 W/cm^2, since their local wick clusters' porosities on the evaporator were very similar, as shown in Figure 13. As mentioned in CHAPTER 2, the capillary limit is important to evaluate the performance of a heat pipe/vapor chamber. The capillary limit is determined by many factors, such as the device's geometry, properties of wick and working liquid. Most of the factors are approximately equivalent for the vapor chamber samples, including the capillary pressure due to the similar porosity of the local wick cluster. The factor that affects the vapor chambers differently is the permeability, which is determined by the porosity and spacing of the wick cluster. Permeability affects the capillary limit significantly if the liquid pressure drop is the dominant component of the total pressure drop of a vapor chamber. However, the vapor pressure drop is the dominate component, due to the submillimeter thick vapor core. Hence, the dryout heat fluxes of the samples were nearly the same, or very close. More information about the effect of vapor core thickness on an ultrathin heat pipe/vapor chamber can be found in [48].

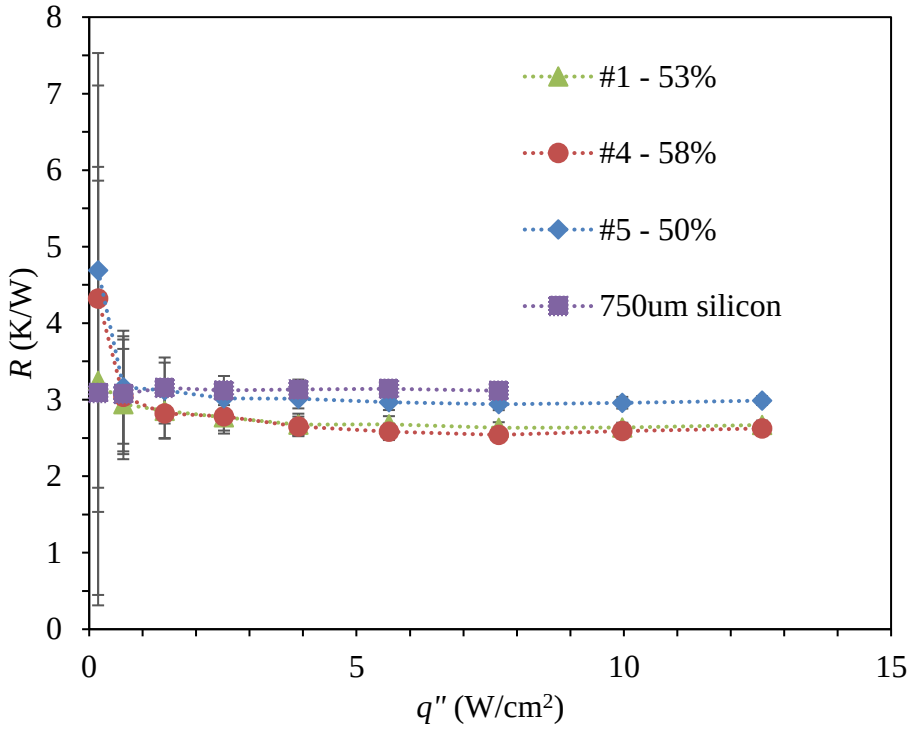

Figure 23. Comparisons of vapor chambers with different porosities

4.3 Extended Thermal Performance Test

Continuous testing for 120 hrs was conducted at a heat flux of 2.5 W/cm^2 to evaluate the long-term performance of the fabricated vapor chambers. The sample mass before and after the test were recorded by a precision balance, with an uncertainty of ±0.1 mg as mentioned in CHAPTER 3. Table 6 shows the mass changes in mg, and as a percentage of the initially charged liquid in the vapor chambers. Figure 24 shows the results for all samples. Usually, the performance of a heat pipe/vapor chamber degrades over time, due to the increased non-condensable gasses, and air leakage into the chamber, but no significant degradation of the performance was observed for the samples during the tests,

and their mass changes were within the measurement uncertainty. This indicates that the fabrication using the UV adhesives, the bonding using the low outgassing epoxy, and the tube attachments using the epoxy following the described procedures were promising in the short-term. Longer duration tests are required to determine further changes in their performance. The adhesion between the UV adhesives and the copper particles and the silicon substrate, under longer term exposure to water also needs further investigation.

Table 6. The mass changes of the samples

#	Mass change, mg (%)
1	0.0 (0.0%)
2	0.1 (0.0049%)
3	0.0 (0.0%)
4	0.1 (0.0050%)
5	-0.1 (-0.0050%)

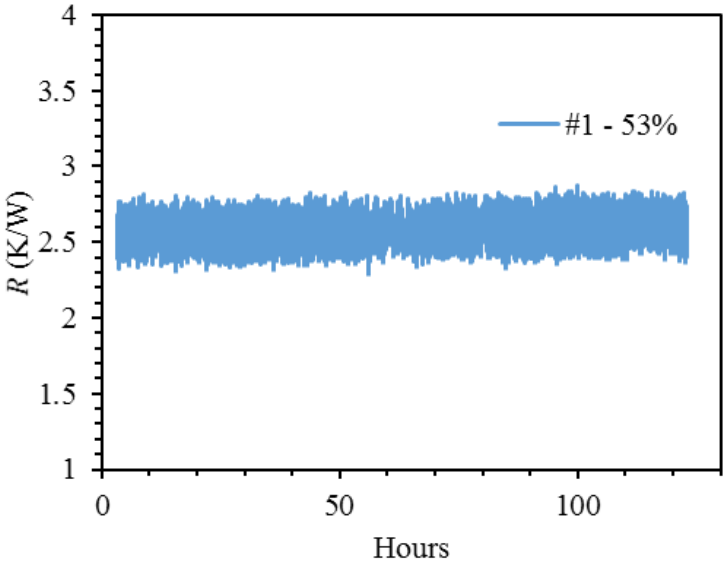
4
3.5
3
2.5
2
1.5
1
R (K/W)
#1 - 53%
0
50
100
Hours

(a)

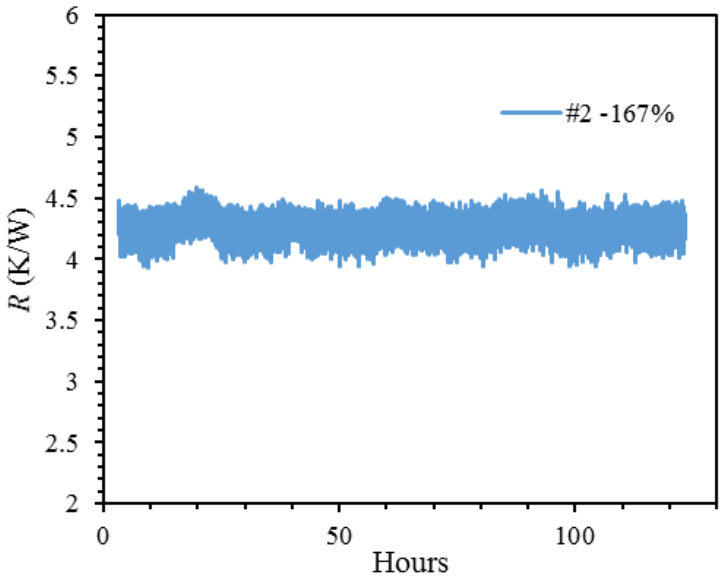
6
5.5
5
4.5
4
3.5
3
2.5
2
R (K/W)
#2 -167%
0
50
100
Hours

(b)

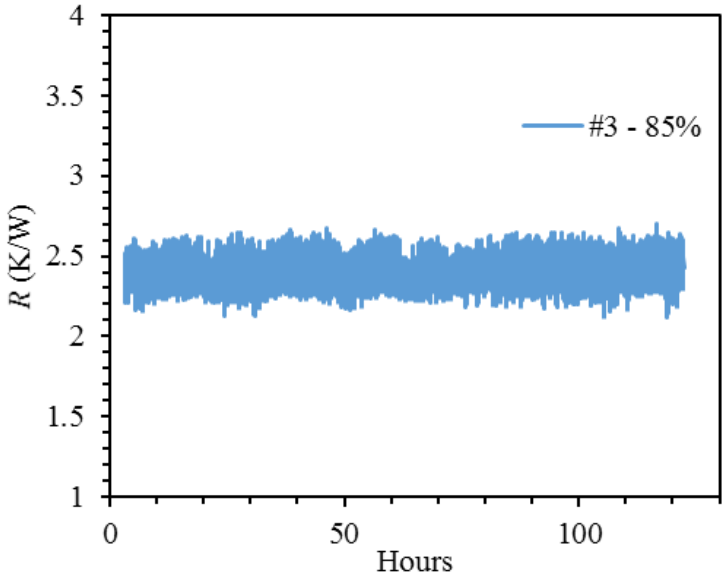
4
3.5
3
2.5
2
1.5
1
R (K/W)
0
50
100
Hours
#3 - 85%

(c)

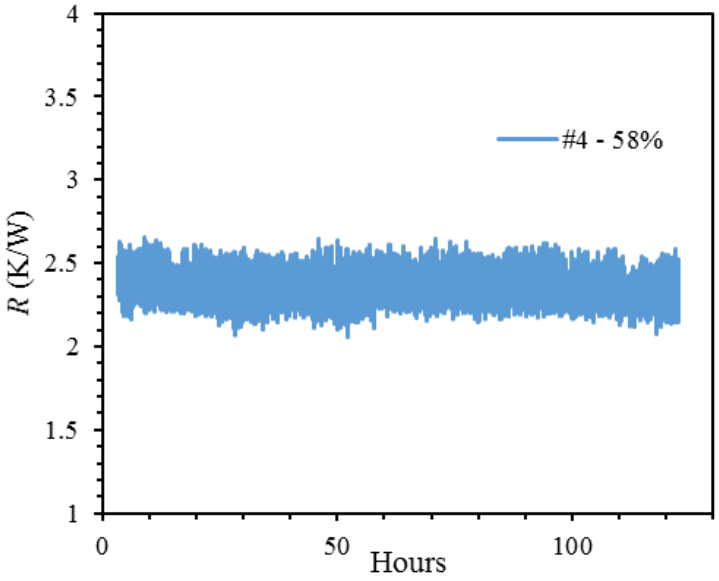
4
3.5
3
2.5
2
1.5
1
R (K/W)
0
50
100
Hours
#4 - 58%

(d)

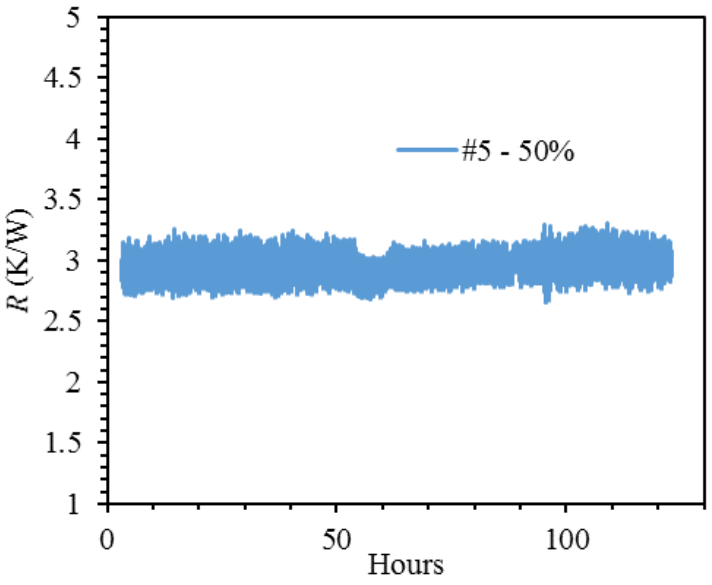

(e)

Figure 24. Performance of the samples over 120 hrs with an uncertainty of ± 0.2 K/W

4.4 Validation of the Experimental Results

4.4.1 A simplified 3-D heat conduction model

A simplified, three-dimensional, steady-state heat conduction model was developed to validate the experimental results. A vapor chamber with dimensions and layer thicknesses shown in Figure **15** and Table 4 respectively, was modeled. A heat flux was applied at the back surface of the vapor chamber to represent the heater. A constant temperature boundary condition was assumed at the condensation region. Perfect insulation was applied to all other surfaces. Figure 25 shows the boundary conditions for the vapor chamber model. In the figure, there are two 6 mm x 6 mm blocks located at the

diagonal corners of the 20 mm x 20 mm top surface. They represent the areas of the epoxy used for securing the vacuum and charging tubes, and they were also thermally insulated in the model.

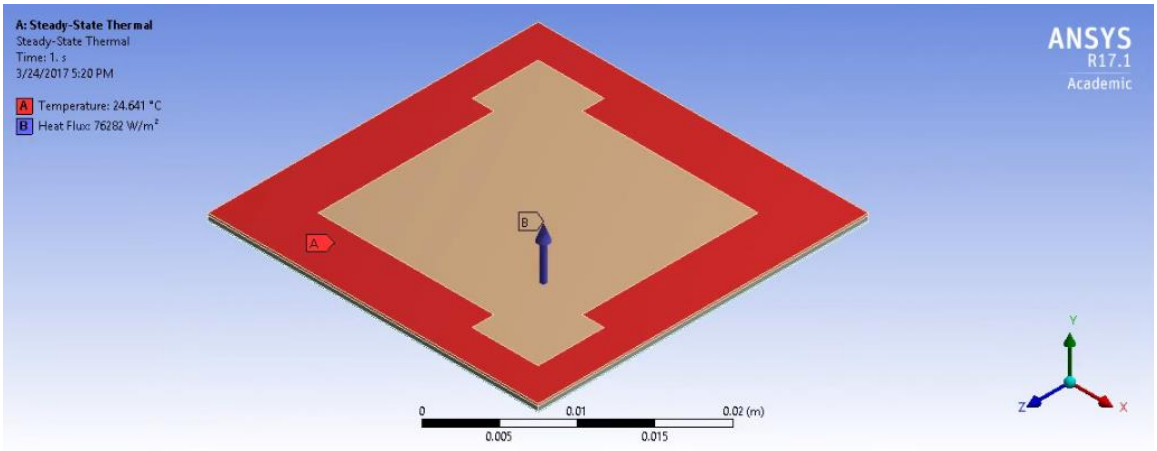

Figure 25. Boundary conditions for the vapor chamber

The material properties used in the model are summarized in Table 7, with assumptions that they are constant and uniform. Equation 15 and Equation 17 [10] were used to estimate the thermal conductivities of the wick and vapor respectively.

$$k_{vapor} = \frac{{h_{fg}}^2 p_v \rho_v {d_v}^2}{12 R_v \mu_v {T_{sat}}^2} \tag{18}$$

where h_{fg} is the latent heat of vaporization, p_v is the vapor saturation pressure, ρ_v is the density, d_v is the vapor core thickness, R_v is the gas constant, μ_v is the dynamic viscosity, and T_{sat} is the saturation temperature. The saturation temperature of vapor was assumed to be the same as the condensation temperature of the vapor chamber.

Table 7. Material properties

Material	Density, kg/m^3	Thermal conductivity, W/m-K	Specific heat, J/kg-K
Silicon	2330	148	712
Wick	8978	Equation 15	381
Vapor	Based on T_{sat}	Equation 17	Based on T_{sat}

The vapor chamber Sample #1 at a porosity of 0.546 was modeled for validation due to its uniform and sintered-like wick structure. Different cases were considered to evaluate the model, as summarized in Table 8. The condensation temperatures of Sample #1 and the corresponding vapor thermal conductivities are summarized in Table 9.

Table 8. Three cases for 3 – D conduction model validation

Case	Wick thermal conductivity, W/m-K	Vapor thermal conductivity, W/m-K
1	2.1	Equation 17
2	22	Equation 17
3	2.1	$\frac{1}{16.4}$ ∗Equation 17

where 22 W/m-K in Case 2 was the thermal conductivity of the sintered powder wick reported in [10], and the constant $\frac{1}{16.4}$ in case 3 was calculated based on the empirical result [10] and the theoretical result using Equation 17, at a temperature of 80 ^{o}C.

Table 9. Properties of vapor for Sample #1

Heat flux, W/cm^2	0.17	0.64	1.41	2.51	3.90	5.58	7.63
Condensation temperature, ^{o}C	21.3	21.0	22.1	22.2	22.9	23.6	24.6
Vapor thermal conductivity, W/m-K (Eq 17)	802	782	876	883	950	1022	1142

The following figure shows the result of the 3-D heat conduction model.

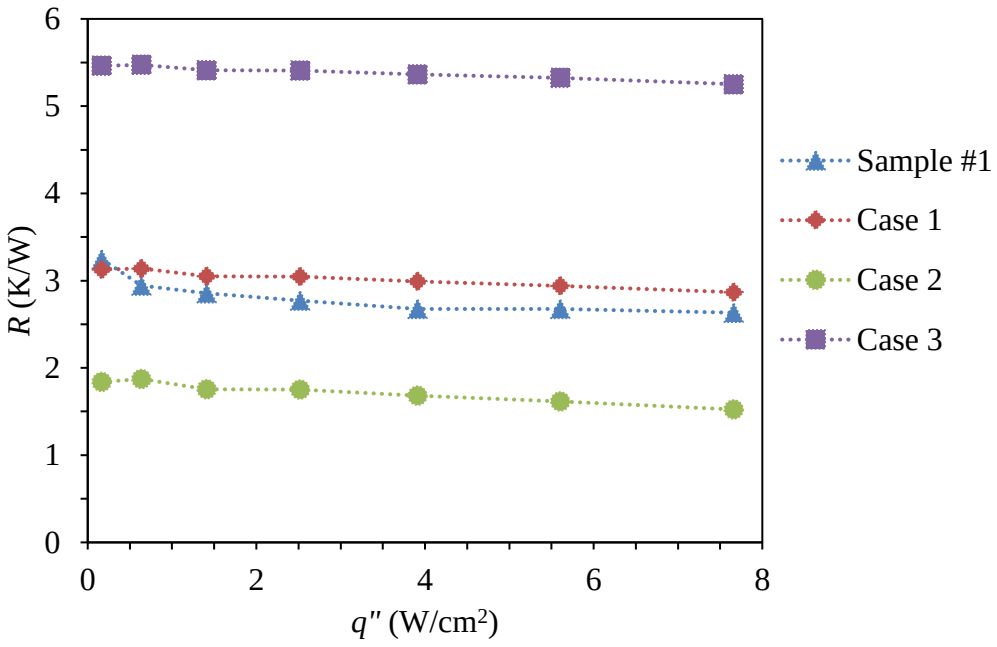

Figure 26. Result of the 3-D heat conduction model

Figure 26 shows that Case 1 has a very good prediction of the experimental result. However, it does not mean that the estimated thermal conductivities of the wick and vapor are their actual values during the tests. If the actual thermal conductivity of the wick is higher than 2.1 W/m-K, the performance of the vapor chamber will be improved, as shown in Case 2. If the actual thermal conductivity of vapor is lower than the theoretical value, the performance of the vapor chamber will be downgraded, as shown in Case 3. Hence, the properties of the wick and vapor are very important to predict the performance of the vapor chamber. The current model can only be used to predict the performance by roughly estimating where it can be bounded. To accurately predict the performance of the vapor chamber, additional experiments are required to investigate the characteristics and properties of the wick and vapor, and a more detailed model, incorporating the details of vapor flow in the core, and liquid flow in the wick, should be developed.

4.4.2 A simplified 1-D thermal resistance network

A simplified 1-D thermal resistance network shown in Figure 27 was developed to estimate the overall performance of the vapor chamber. The components included are: 1) the conduction and spreading resistance of the bottom 20 mm x 20 mm substrate; 2) conduction and spreading resistance of the wick structure; 3) evaporation resistance at the evaporator; 4) conduction resistance of the vapor core; 5) condensation resistance at the condenser; and 6) spreading resistance of the top 30 mm x 30 mm substrate.

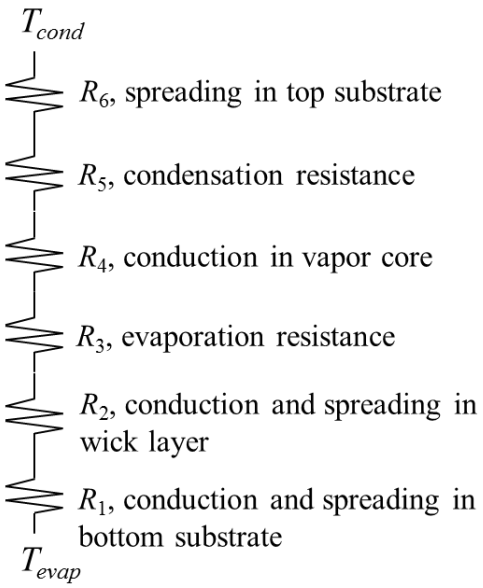

Figure 27. 1–D thermal resistance network for the vapor chamber

The numerical method described in [49] was used to compute the total thermal resistance of the bottom substrate and wick layer, and the thermal resistance of the wick layer was then derived from this total thermal resistance. Based on the given properties from the previous sections, the spreading resistances were computed using the method given in [50], and the conduction resistances were based on 1-D conduction. The evaporation and condensation resistances were estimated using a heat transfer coefficient of 10^6 W/m^2-K [49]. Under a heat flux of 7.63 W/cm^2 and a vapor effective thermal conductivity of 1142 W/m-K from Table 9, three cases were studied to evaluate the effect of wick layer on the performance of the vapor chamber, as summarized in Table 10. The result is compared to Sample #1, as shown in Figure 28.

Table 10. Three cases for 1–D thermal resistance network study

Case	Thickness of wick layer, µm	Wick thermal conductivity, W/m-K
1	85	2.1
2	85	4.2
3	42.5	2.1

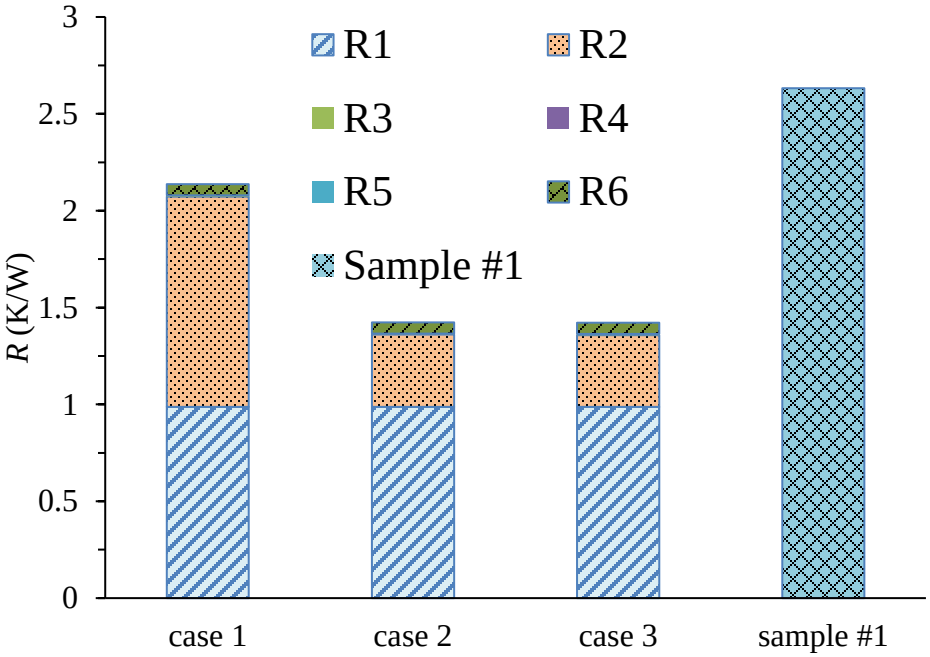

Figure 28. Result of the 1 – D thermal resistance network

As shown in Figure 28, the bottom substrate and the wick layer are the two major components that contribute more than 95% of the thermal resistance of the vapor chamber.

In Case 1, the wick layer contributes more than 50% of the total thermal resistance. By doubling the thermal conductivity of the wick or reducing the wick layer's thickness by half, it reduces to approximately 25% of the total thermal resistance. This indicates that the thermal conductivity and thickness of the wick have significant effects on the performance of the vapor chamber. As discussed in the previous section, accurately estimated properties of the wick are expected to provide a significantly improved prediction of the performance and thus, a more accurate analysis of the contributions of the components to the total thermal resistance of the vapor chamber. Also, there were contact resistances between the thermocouples and the evaporator and condenser during the measurements. By considering the contact resistances in the thermal resistance network, the predicted thermal resistance will be more accurate and higher.

4.5 In Comparison to Recent Studies

The performance of the thin silicon vapor chamber in this study is reasonable and comparable to the published data from Table 1. Figure 29 shows the dryout heat flux and total thermal resistance, and Figure 30 shows the thickness of vapor core and wick structure layer, for each study with the total thickness. The vapor chamber in this study has a wick structure and vapor core thickness that are thinner than that of studies from [2, 4, 7], but performs better or similarly in term of dryout heat flux. A thick wick structure layer leads to a high permeability and low liquid pressure drop and thus, a high heat transfer rate according to Equation 16, and a thin vapor core leads to a high vapor pressure drop according to Equation 8. Also, most of the studies used liquid cooled blocks as heat sinks under different heating and cooling configurations, as summarized in Table 1. For example, the silicon vapor chamber [6] and silicon heat pipe [8] had heating and cooling

configurations 2 and 3 respectively (see Figure 4), used liquid cooled copper blocks and short thermal paths to reject heat to the ambient and thus, presented high dryout heat fluxes and low thermal resistances. While vapor chambers in [2] and [4] had a cooling and heating configuration 1 (see Figure 4), presented a low dryout heat flux. Hence, the vapor chamber in this study that ranks 2nd in thinness, achieves a better or comparable performance to these studies, based on considering the geometry, wick structure, working fluid, wick saturation ratio, and heating and cooling configuration.

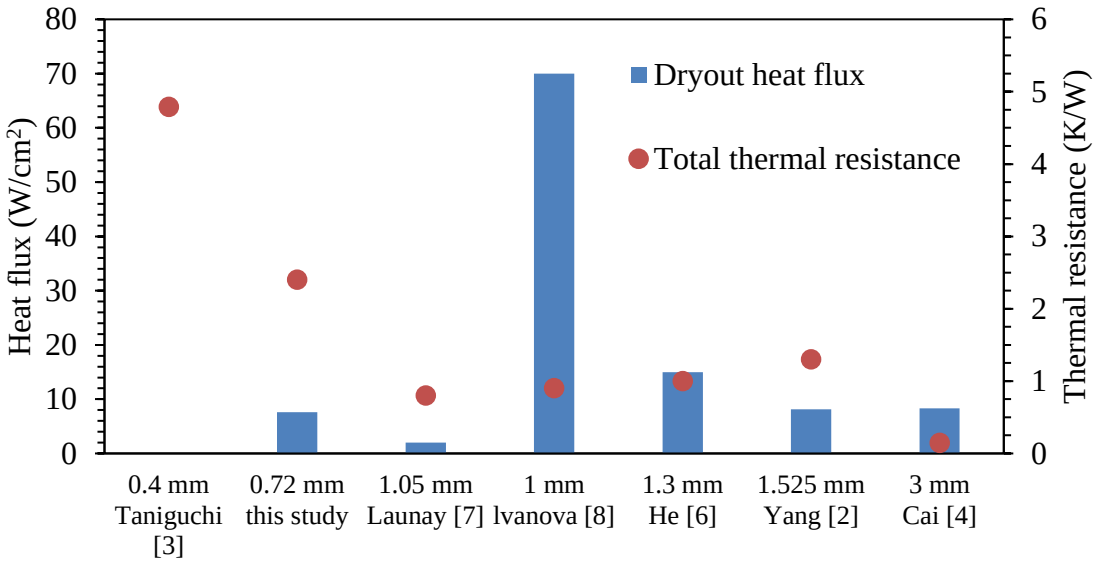

Figure 29. Comparison to recent studies in term of performance

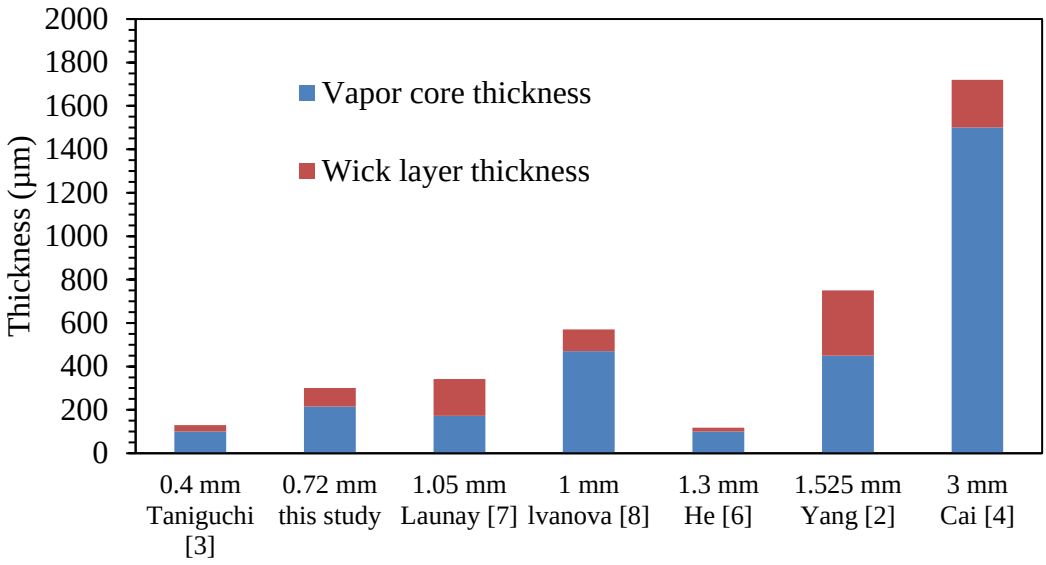

Figure 30. Comparison to recent studies in term of thicknesses

CHAPTER 5. CONCLUSIONS AND FUTURE WORK

5.1 Conclusions

Thermal management for portable electronics is important, especially as system sizes continue to shrink, and heterogeneous integration is utilized. Inadequate attention to thermal management can cause performance, reliability, safety, and user comfort issues. Vapor chamber integrated into interposers can be a promising solution to the problem. This thesis studies submillimeter thick vapor chambers, by reviewing the fundamentals, designing, fabricating, testing and modeling. It aims to develop a vapor chamber suitable for integration into interposer for heat spreading, and performs better than solid silicon heat spreaders.

From the Surface evolver modeling, the spherical powder wick in hexagonal array was found to have the highest capillary performance, among the wick structures studied. By balancing the capillary pressure, permeability, and thermal conductivity of the wick structure, an optimal design of the wick structure can be obtained. Using inkjet printing and self-assembly, a bi-porous monolayer copper power wick structure suitable for the vapor chamber, due to its high capillary pressure, high permeability and low resistance, was created.

The charging station developed in this study provided a reliable and precise approach to charge the vapor chamber. The turbomolecular pump can evacuate the vapor chamber to a very high vacuum level of 1.2 Pa, and the peristaltic pump can supply liquid at a rate as low as 1 μl/min. As seen from the calibration and vapor chamber charging

results, the charging station operated in a very stable manner. The largest uncertainty in wick saturation ratio was ± 6% or ± 2.5 µl. Hence, the charging station is suitable for vapor chambers.

Multiple tests were performed to evaluate the performance of vapor chamber samples. The wick saturation ratio test showed that the amount of liquid charged in the vapor chambers significantly affected their performance. The lowest thermal resistance of a charged sample was about 2.4 K/W at 5.6 W/cm^2, which was about 38% of the uncharged sample's, and 74% of the solid silicon substrate's thermal resistance. Oversaturation downgraded the performance due to the reduced thin film evaporation and vapor core thickness. An optimal wick saturation ratio was found to be approximately 50%, which provided the vapor chambers with the highest dryout heat flux of 7.6 W/cm^2, since this ratio created the highest capillary pressure for the close packed sphere wicks. The sample with a wick saturation ratio of 85% showed the lowest thermal resistance of 2.4 K/W, since it had the best balance between the liquid free surface area and the thin film percentage, which produced larger film evaporation area than others. This agreed with the findings reported in [36].

From the porosity test, Sample #4 showed that an optimal balance between the capillary pressure, permeability and effective thermal conductivity of the wick structure, which resulted in a thermal resistance of 2.5 K/W at 7.6 W/cm^2, is important. The vapor chamber performance was found to be stable, with minimal change in mass, over a 120 hours test. Much longer performance tests are required to assess the viability of the bonding material and techniques used in this work. Overall, the tests showed that the charged vapor chambers performed better than a solid silicon substrate of identical thickness, and can

potentially be integrated into interposer for heat spreading, as a solution to the thermal management of portable electronics.

5.2 Future work

This study can be improved in many areas, such as the fabrication, experiment, and modeling. The following are the recommended works.

Additional tests are needed to evaluate the UV adhesive under a long-term exposure to air and water. The thermal performance and the mass change of the vapor chamber need to be evaluated under a much longer period of testing, for example, 20000 hours [51]. The UV adhesive was used to attach the powdered copper particles to the silicon chamber. Long-term exposure to water at a high temperature may change their adhesion, and the vapor chamber's performance.

Visualization of the working liquid and wick structure inside a vapor chamber can be performed by creating a glass window on the top surface, or using a glass wafer serving as the top substrate of the vapor chamber. Using a high-speed camera to visualize conditions inside the vapor chamber through the glass can capture how liquid is returned through the capillary action, how heat is transferred through the thin film evaporation, and how much and where the thin films are formed on the wick structure. It can also explain where and how the dryout initiates, and how it is impacted by heat input. By performing such visualization, we can have better understanding about the wick structure and vapor chamber operation.

New test setups and experiments, such as the mass transport experimental test [52] or the vacuum chamber test [34], and the rising liquid test [19] are needed to evaluate the properties of the wick structure and vapor. A more detailed model using results from these tests can be developed, in order to get a better simulation and prediction of the vapor chamber's performance. More wick patterns can also be investigated to see how they affect the vapor chamber.

The fabrication process can be improved in many areas. Graphene ink or CNT ink can be used to attach the powder copper particles to the silicon chamber instead of the UV adhesive. Graphene ink and CNT ink can withstand a much higher temperature than the UV adhesive. Therefore, bonding the vapor chamber can be performed in a high temperature environment, such as eutectic bonding and anodic bonding, and solder can be used to secure the vacuum and charging tubes. A better sealing can be obtained from these changes. Heaters and temperature sensors can also be fabricated on the vapor chamber to obtain more accurate measurements. We can also change the size of the vapor chamber by changing the dimensions of the chamber, the dimensions of the peripheral extension, the walls thicknesses, the vapor core thickness, and the size of the powder/wick. We can also change the size and location of the heater to see how they affect the vapor chamber.

The charging station can be improved by changing the fittings between the Tygon tube and the stainless steel/copper tube from epoxy to vacuum fittings. It is difficult to find a fitting that directly connect a plastic and metal tubing, and prevent vacuum leakage at the same time. A better connection configuration needs to be developed so epoxy can be removed from the charging station. More pressure gauges can be installed at different

locations on the station, so we can have more information about an operating charging station.

APPENDIX A. SURFACE EVOLVER CODE

A.1 Cylindrical pillar, squared array

```
parameter  r_1 = 1          //radius of the cylinder
parameter  h_1 = 2          //height of column
parameter  h_2 = 1  //height of meniscus
parameter  p_1 = 3          //pitch
parameter an = 45           //contact angle
#define WALLT (cos(an*pi/180))

quantity mci info_only global_method
sq_mean_curvature global

gravity_constant 0

constraint 1
formula: x^2+y^2=r_1^2
constraint 2
formula: x^2+y^2=r_1^2
energy:
e1:  -WALLT*z*y/r_1
e2:  WALLT*z*x/r_1
e3:   0
constraint 3
formula: abs(x)+abs(y) = p_1/2^0.5
constraint 5
formula: x = p_1/2^0.5
constraint 6
formula: y = 0
constraint 7
formula: x = 0
constraint 8
formula: y = p_1/2^0.5
constraint 9
formula: x = -p_1/2^0.5
constraint 10
formula: y = -p_1/2^0.5
constraint 11 nonnegative
formula: z


vertices
//column top
1  r_1  0  h_1      constraint 1 fixed
2  0  r_1  h_1      constraint 1 fixed
3  -r_1 0  h_1      constraint 1 fixed
4  0 -r_1  h_1      constraint 1 fixed
//column bottom
15  r_1  0  0       constraint 1 fixed
16  0  r_1  0       constraint 1 fixed
17  -r_1 0  0       constraint 1 fixed
18  0 -r_1  0       constraint 1 fixed

//meniscus
7  r_1*cos(45*pi/180)  r_1*sin(45*pi/180)  h_2             constraint 2
8  -r_1*cos(45*pi/180) r_1*sin(45*pi/180)  h_2             constraint 2
```

```
9  -r_1*cos(45*pi/180) -r_1*sin(45*pi/180) h_2              constraint 2
10 r_1*cos(45*pi/180)  -r_1*sin(45*pi/180) h_2              constraint 2
11  p_1/2^0.5  0  h_2      constraint 3,5,6,11
12  0  p_1/2^0.5  h_2      constraint 3,7,8,11
13  -p_1/2^0.5 0  h_2      constraint 3,9,6,11
14  0 -p_1/2^0.5  h_2      constraint 3,7,10,11
//meniscus base
19  p_1/2^0.5  0  0        fixed
20  0  p_1/2^0.5  0        fixed
21  -p_1/2^0.5 0  0        fixed
22  0 -p_1/2^0.5  0        fixed

edges
//column
1 1 2         constraint 1 fixed
2 2 3         constraint 1 fixed
3 3 4         constraint 1 fixed
4 4 1         constraint 1 fixed
5 15 16       constraint 1 fixed
6 16 17       constraint 1 fixed
7 17 18       constraint 1 fixed
8 18 15       constraint 1 fixed
9 15 1        fixed
10 16 2       fixed
11 17 3       fixed
12 18 4       fixed
//meniscus
13 11 12      constraint 3,11
14 12 7
15 7 11
16 12 8
17 8 7        constraint 2
18 12 13      constraint 3,11
19 13 8
20 13 9
21 9 8        constraint 2
22 13 14      constraint 3,11
23 14 9
24 14 10
25 10 9       constraint 2
26 14 11      constraint 3,11
27 11 10
28 7 10       constraint 2
//menicus base
29 19 20      fixed
30 20 21      fixed
31 21 22      fixed
32 22 19      fixed

faces
////cylinder
//1 1 2 3 4          color gray fixed no_refine bare
//2 5 6 7 8          color gray fixed no_refine bare
//3 -9 5 10 -1       constraint 1 color black fixed no_refine bare
//4 -10 6 11 -2      constraint 1 color black fixed no_refine bare
//5 -11 7 12 -3      constraint 1 color black fixed no_refine bare
//6 -12 8 9 -4       constraint 1 color black fixed no_refine bare
////meniscus base
//7 29 30 31 32 fixed no_refine color blue bare
//meniscus
9  13 14 15  constraint 11 color blue
10 -14 16 17 constraint 11 color blue
11 -16 18 19 constraint 11 color blue
```

```
12 -19 20 21  constraint 11 color blue
13 -20 22 23  constraint 11 color blue
14 -23 24 25  constraint 11 color blue
15 -24 26 27  constraint 11 color blue
16 -27 -15 28 constraint 11       color blue

bodies
1 9 10 11 12 13 14 15 16 volume (h_2*((p_1)^2-pi*r_1^2))

s
10r
3d
q
```

A.2 Cylindrical pillar, hexagonal array

```
parameter  r_1 = 1          //radius of the cylinder
parameter  h_1 = 4          //height of column
parameter  h_2 = 0.5              //height of meniscus
parameter  p_1 = 3          //pitch
parameter an = 45           //contact angle
#define WALLT (-cos(an*pi/180))
quantity mci info_only global_method
mean_curvature_integral
gravity_constant 0

constraint 1
formula: x^2+y^2=r_1^2

constraint 2
formula: x^2+y^2=r_1^2
energy:
e1:  -WALLT*z*y/r_1
e2:  WALLT*z*x/r_1
e3:   0

//meniscus outside edge constraints
constraint 3
formula: y = -tan(30*pi/180)*x + p_1/2/cos(30*pi/180)
constraint 4
formula: y = tan(30*pi/180)*x + p_1/2/cos(30*pi/180)
constraint 5
formula: x = -p_1/2
constraint 6
formula: y = -tan(30*pi/180)*x - p_1/2/cos(30*pi/180)
constraint 7
formula: y = tan(30*pi/180)*x - p_1/2/cos(30*pi/180)
constraint 8
formula: x = p_1/2
//meniscus outside point constraints
constraint 9
formula: x = p_1/2
constraint 10
formula: y = p_1/2*tan(30*pi/180)
constraint 11
formula: x = 0
constraint 12
formula: y = p_1/2/cos(30*pi/180)
constraint 13
formula: x = -p_1/2
```

```
constraint 14
formula: y = -p_1/2*tan(30*pi/180)
constraint 15
formula: y = -p_1/2/cos(30*pi/180)

vertices
//column top
1   r_1   0   h_1       constraint 1 fixed
2   0   r_1   h_1       constraint 1 fixed
3   -r_1 0   h_1       constraint 1 fixed
4   0 -r_1   h_1       constraint 1 fixed
//column bottom
25   r_1   0   0       constraint 1 fixed
26   0   r_1   0       constraint 1 fixed
27   -r_1 0   0       constraint 1 fixed
28   0 -r_1   0       constraint 1 fixed

//meniscus
7       r_1*cos(30*pi/180)   r_1*sin(30*pi/180)   h_2    constraint 2
8       0                    r_1                   h_2    constraint 2
9       -r_1*cos(30*pi/180)  r_1*sin(30*pi/180)   h_2    constraint 2
10      -r_1*cos(30*pi/180)  -r_1*sin(30*pi/180)  h_2    constraint 2
11      0                    -r_1                  h_2    constraint 2
12      r_1*cos(30*pi/180)   -r_1*sin(30*pi/180)  h_2    constraint 2

13      p_1/2   p_1/2*tan(30*pi/180)              h_2    constraint 9,10
14      0       p_1/2/cos(30*pi/180)              h_2    constraint 11,12
15      -p_1/2  p_1/2*tan(30*pi/180)              h_2    constraint 13,10
16      -p_1/2  -p_1/2*tan(30*pi/180)      h_2    constraint 13,14
17      0       -p_1/2/cos(30*pi/180)      h_2    constraint 11,15
18      p_1/2   -p_1/2*tan(30*pi/180)      h_2    constraint 9,14
//mesnicus base
19      p_1/2   p_1/2*tan(30*pi/180)              0      fixed
20      0       p_1/2/cos(30*pi/180)              0      fixed
21      -p_1/2  p_1/2*tan(30*pi/180)              0      fixed
22      -p_1/2  -p_1/2*tan(30*pi/180)      0      fixed
23      0       -p_1/2/cos(30*pi/180)      0      fixed
24      p_1/2   -p_1/2*tan(30*pi/180)      0      fixed

edges
//column
1 1 2         constraint 1 fixed
2 2 3         constraint 1 fixed
3 3 4         constraint 1 fixed
4 4 1         constraint 1 fixed
5 25 26       constraint 1 fixed
6 26 27       constraint 1 fixed
7 27 28       constraint 1 fixed
8 28 25       constraint 1 fixed
9 25 1        fixed
10 26 2       fixed
11 27 3       fixed
12 28 4       fixed
//meniscus
13 7 8        constraint 2
14 8 9        constraint 2
15 9 10       constraint 2
16 10 11      constraint 2
17 11 12      constraint 2
18 12 7       constraint 2
19 13 14      constraint 3
20 14 15      constraint 4
21 15 16      constraint 5
```

```
22 16 17      constraint 6
23 17 18      constraint 7
24 18 13      constraint 8
25 13 7
26 14 8
27 15 9
28 16 10
29 17 11
30 18 12
//meniscus base
31 19 20      fixed
32 20 21      fixed
33 21 22      fixed
34 22 23      fixed
35 23 24      fixed
36 24 19      fixed

faces
//meniscus
1 19 26 -13 -25     color blue
2 20 27 -14 -26     color blue
3 21 28 -15 -27     color blue
4 22 29 -16 -28     color blue
5 23 30 -17 -29     color blue
6 24 25 -18 -30     color blue
////meniscus base
//7 31 32 33 34 35 36 fixed no_refine color blue bare
////cylinder
//8 1 2 3 4         color black fixed no_refine bare
//9 5 6 7 8         color black fixed no_refine bare
//10 -9 5 10 -1           constraint 1 color black fixed no_refine bare
//11 -10 6 11 -2    constraint 1 color black fixed no_refine bare
//12 -11 7 12 -3    constraint 1 color black fixed no_refine bare
//13 -12 8 9 -4     constraint 1 color black fixed no_refine bare

bodies
1 1 2 3 4 5 6 volume ((3^0.5/2*p_1^2-pi*r_1^2)*h_2)

s
10r
3d
q
```

A.3 Spherical powder, squared array

```
parameter  r_1 = 1         //radius
parameter  h_1 = 0.5             //meniscus height
parameter  p_1 = 3         //pitch
parameter an = 45          //contact angle
#define WALLT (cos(an*pi/180))
#define rs (r_1^2-(r_1-h_1)^2)^0.5

gravity_constant 0

constraint 1
formula: x^2+y^2+(z-r_1)^2=r_1^2
constraint 2
formula: x^2+y^2+(z-r_1)^2=r_1^2
energy:
```

```
e1:  -WALLT*z*y/((x)^2+(y)^2)^0.5
e2:  WALLT*z*x/((x)^2+(y)^2)^0.5
e3:  0
constraint 3
formula: abs(x)+abs(y) = p_1/2^0.5

constraint 5
formula: x = p_1/2^0.5
constraint 6
formula: y = 0
constraint 7
formula: x = 0
constraint 8
formula: y = p_1/2^0.5
constraint 9
formula: x = -p_1/2^0.5
constraint 10
formula: y = -p_1/2^0.5
constraint 11 nonnegative
formula: z

vertices
1  r_1  0  r_1  constraint 1 fixed
2  0  r_1  r_1  constraint 1 fixed
3  -r_1 0  r_1  constraint 1 fixed
4  0 -r_1  r_1  constraint 1 fixed
5  0  0  2*r_1 constraint 1 fixed
6  0  0 0 constraint 1 fixed
//meniscus
7  rs*cos(45*pi/180)  rs*sin(45*pi/180)  h_1 constraint 2
8  -rs*cos(45*pi/180) rs*sin(45*pi/180)  h_1 constraint 2
9  -rs*cos(45*pi/180) -rs*sin(45*pi/180) h_1 constraint 2
10 rs*cos(45*pi/180)  -rs*sin(45*pi/180) h_1 constraint 2
11  p_1/2^0.5  0  h_1 constraint 3,5,6,11
12  0  p_1/2^0.5  h_1 constraint 3,7,8,11
13  -p_1/2^0.5 0 h_1 constraint 3,9,6,11
14  0 -p_1/2^0.5  h_1 constraint 3,7,10,11
//meniscus base
15  p_1/2^0.5  0  0 fixed
16  0  p_1/2^0.5  0 fixed
17  -p_1/2^0.5 0  0 fixed
18  0 -p_1/2^0.5  0 fixed

edges
//sphere
1 1 2  constraint 1 fixed
2 2 3  constraint 1 fixed
3 3 4  constraint 1 fixed
4 4 1  constraint 1 fixed
5 5 1  constraint 1 fixed
6 1 6  constraint 1 fixed
7 6 3  constraint 1 fixed
8 3 5  constraint 1 fixed
9  5 4 constraint 1 fixed
10 4 6 constraint 1 fixed
11 6 2 constraint 1 fixed
12 2 5 constraint 1 fixed
//meniscus
13 11 12 constraint 3,11
14 12 7
15 7 11
16 12 8
17 8 7 constraint 2
```

```
18 12 13 constraint 3,11
19 13 8
20 13 9
21 9 8 constraint 2
22 13 14 constraint 3,11
23 14 9
24 14 10
25 10 9 constraint 2
26 14 11 constraint 3,11
27 11 10
28 7 10 constraint 2
//meniscus base
29 15 16 fixed
30 16 17 fixed
31 17 18 fixed
32 18 15 fixed

faces
//sphere
//1  5 -4  -9 constraint 1 fixed no_refine color black bare
//2 -8  3  -9 constraint 1 fixed no_refine color black bare
//3 -12 2  8  constraint 1 fixed no_refine color black bare
//4  5  1  12 constraint 1 fixed no_refine color black bare
//5 -4  10 -6 constraint 1 fixed no_refine color black bare
//6 -3 -7 -10 constraint 1 fixed no_refine color black bare
//7 -2 -11 7  constraint 1 fixed no_refine color black bare
//8 -1  6  11 constraint 1 fixed no_refine color black bare
//meniscus
9  13 14 15 color blue constraint 11
10 -14 16 17 color blue constraint 11
11 -16 18 19 color blue constraint 11
12 -19 20 21  color blue constraint 11
13 -20 22 23  color blue constraint 11
14 -23 24 25  color blue constraint 11
15 -24 26 27  color blue constraint 11
16 -27 -15 28  color blue constraint 11
//meniscus base
//17 29 30 31 32 fixed color blue no_refine  bare

bodies
1 9 10 11 12 13 14 15 16 volume (p_1^2*h_1-1/3*pi*h_1^2*(3*r_1-h_1))

s
10r
3d
q
```

A.4 Spherical powder, hexagonal array

```
parameter  r_1 = 1         //radius
parameter  h_1 = 0.5             //meniscus height
parameter  p_1 = 3         //pitch
parameter an = 45          //contact angle
#define WALLT (-cos(an*pi/180))
#define rs (r_1^2-(r_1-h_1)^2)^0.5

gravity_constant 0

constraint 1
```

```
formula: x^2+y^2+(z-r_1)^2=r_1^2
constraint 2
formula: x^2+y^2+(z-r_1)^2=r_1^2
energy:
e1:  -WALLT*z*y/((x)^2+(y)^2)^0.5
e2:  WALLT*z*x/((x)^2+(y)^2)^0.5
e3:  0

//meniscus outside constraints
constraint 3
formula: y = -tan(30*pi/180)*x + p_1/2/cos(30*pi/180)
constraint 4
formula: y = tan(30*pi/180)*x + p_1/2/cos(30*pi/180)
constraint 5
formula: x = -p_1/2
constraint 6
formula: y = -tan(30*pi/180)*x - p_1/2/cos(30*pi/180)
constraint 7
formula: y = tan(30*pi/180)*x - p_1/2/cos(30*pi/180)
constraint 8
formula: x = p_1/2
//meniscus outside point constraints
constraint 9
formula: x = p_1/2
constraint 10
formula: y = p_1/2*tan(30*pi/180)
constraint 11
formula: x = 0
constraint 12
formula: y = p_1/2/cos(30*pi/180)
constraint 13
formula: x = -p_1/2
constraint 14
formula: y = -p_1/2*tan(30*pi/180)
constraint 15
formula: y = -p_1/2/cos(30*pi/180)

constraint 16 nonnegative
formula: z

vertices
1  r_1  0  r_1  constraint 1 fixed
2  0  r_1  r_1  constraint 1 fixed
3  -r_1 0  r_1  constraint 1 fixed
4  0 -r_1  r_1  constraint 1 fixed
5  0  0  2*r_1 constraint 1 fixed
6  0  0 0 constraint 1 fixed
//meniscus
7      rs*cos(30*pi/180)   rs*sin(30*pi/180)   h_1    constraint 2
8      0                   rs                  h_1    constraint 2
9      -rs*cos(30*pi/180)  rs*sin(30*pi/180)   h_1    constraint 2
10     -rs*cos(30*pi/180)  -rs*sin(30*pi/180)  h_1    constraint 2
11     0                   -rs                 h_1    constraint 2
12     rs*cos(30*pi/180)   -rs*sin(30*pi/180)  h_1    constraint 2

13     p_1/2  p_1/2*tan(30*pi/180)             h_1    constraint 9,10,16
14     0      p_1/2/cos(30*pi/180)             h_1    constraint 11,12,16
15     -p_1/2 p_1/2*tan(30*pi/180)             h_1    constraint 13,10,16
16     -p_1/2 -p_1/2*tan(30*pi/180)      h_1    constraint 13,14,16
17     0      -p_1/2/cos(30*pi/180)      h_1    constraint 11,15,16
18     p_1/2  -p_1/2*tan(30*pi/180)      h_1    constraint 9,14,16
//mesnicus base
19     p_1/2  p_1/2*tan(30*pi/180)             0      fixed
```

```
20     0      p_1/2/cos(30*pi/180)              0      fixed
21     -p_1/2 p_1/2*tan(30*pi/180)              0      fixed
22     -p_1/2 -p_1/2*tan(30*pi/180)      0      fixed
23     0      -p_1/2/cos(30*pi/180)      0      fixed
24     p_1/2  -p_1/2*tan(30*pi/180)      0      fixed


edges
//sphere
1 1 2  constraint 1 fixed
2 2 3  constraint 1 fixed
3 3 4  constraint 1 fixed
4 4 1  constraint 1 fixed
5 5 1  constraint 1 fixed
6 1 6  constraint 1 fixed
7 6 3  constraint 1 fixed
8 3 5  constraint 1 fixed
9  5 4 constraint 1 fixed
10 4 6 constraint 1 fixed
11 6 2 constraint 1 fixed
12 2 5 constraint 1 fixed
//meniscus
13 7 8        constraint 2
14 8 9        constraint 2
15 9 10       constraint 2
16 10 11      constraint 2
17 11 12      constraint 2
18 12 7       constraint 2
19 13 14      constraint 3,16
20 14 15      constraint 4,16
21 15 16      constraint 5,16
22 16 17      constraint 6,16
23 17 18      constraint 7,16
24 18 13      constraint 8,16
25 13 7
26 14 8
27 15 9
28 16 10
29 17 11
30 18 12
//meniscus base
31 19 20      fixed
32 20 21      fixed
33 21 22      fixed
34 22 23      fixed
35 23 24      fixed
36 24 19      fixed


faces
//sphere
//1  5 -4  -9 constraint 1 fixed no_refine color black bare
//2 -8  3  -9 constraint 1 fixed no_refine color black bare
//3 -12 2  8  constraint 1 fixed no_refine color black bare
//4  5  1  12 constraint 1 fixed no_refine color black bare
//5 -4  10 -6 constraint 1 fixed no_refine color black bare
//6 -3 -7 -10 constraint 1 fixed no_refine color black bare
//7 -2 -11 7  constraint 1 fixed no_refine color black bare
//8 -1  6  11 constraint 1 fixed no_refine color black bare
//meniscus
11 19 26 -13 -25    color blue constraint 16
12 20 27 -14 -26    color blue constraint 16
13 21 28 -15 -27    color blue constraint 16
```

```
14 22 29 -16 -28    color blue constraint 16
15 23 30 -17 -29    color blue constraint 16
16 24 25 -18 -30    color blue constraint 16
//meniscus base
//17 31 32 33 34 35 36 fixed no_refine color blue bare

bodies
1 11 12 13 14 15 16 volume (3^0.5/2*p_1^2*h_1-1/3*pi*h_1^2*(3*r_1-h_1))


s
10r
3d
Q
```

REFERENCES

[1] P. Garrou, M. Koyanagi, and P. Ramm, *Handbook of 3D Integration. 3D Process Technology, vol. 3*: Wiley, New York, 2014.

[2] K.-S. Yang, C.-C. Lin, J.-C. Shyu, C.-Y. Tseng, and C.-C. Wang, "Performance and two-phase flow pattern for micro flat heat pipes," *International Journal of Heat and Mass Transfer*, vol. 77, pp. 1115-1123, 2014.

[3] J. Taniguchi, T. Shioga, and Y. Mizuno, "Si Vapor Chamber Integrated with Through Silicon Via for 3D Packaging," in *International Symposium on Microelectronics*, 2013, pp. 000552-000557.

[4] Q. Cai, B.-c. Chen, and C. Tsai, "Design, development and tests of high-performance silicon vapor chamber," *Journal of Micromechanics and Microengineering*, vol. 22, p. 035009, 2012.

[5] Q. Cai, A. Bhunia, C. Tsai, M. W. Kendig, and J. F. DeNatale, "Studies of material and process compatibility in developing compact silicon vapor chambers," *Journal of Micromechanics and Microengineering*, vol. 23, p. 065003, 2013.

[6] B. He, M. Wei, S. Somasundaram, C. S. Tan, and E. N. Wang, "Experiments on the ultrathin silicon vapor chamber for enhanced heat transfer performance," in *Thermal and Thermomechanical Phenomena in Electronic Systems (ITherm), 2016 15th IEEE Intersociety Conference on*, 2016, pp. 569-573.

[7] S. Launay, V. Sartre, and M. Lallemand, "Experimental study on silicon micro-heat pipe arrays," *Applied Thermal Engineering*, vol. 24, pp. 233-243, 2004.

[8] M. Ivanova, A. Lai, C. Gillot, N. Sillon, C. Schaeffer, F. Lefevre, *et al.*, "Design, fabrication and test of silicon heat pipes with radial microcapillary grooves," in *Thermal and Thermomechanical Proceedings 10th Intersociety Conference on Phenomena in Electronics Systems, 2006. ITHERM 2006.*, 2006, pp. 545-551.

[9] D. Khrustalev and A. Faghri, "Thermal characteristics of conventional and flat miniature axially grooved heat pipes," *Journal of Heat transfer*, vol. 117, pp. 1048-1054, 1995.

[10] R. S. Prasher, "A simplified conduction based modeling scheme for design sensitivity study of thermal solution utilizing heat pipe and vapor chamber technology," *Journal of Electronic Packaging*, vol. 125, pp. 378-385, 2003.

[11] U. Vadakkan, S. V. Garimella, and J. Y. Murthy, "Transport in flat heat pipes at high heat fluxes from multiple discrete sources," *Journal of heat transfer,* vol. 126, pp. 347-354, 2004.

[12] B. Xiao and A. Faghri, "A three-dimensional thermal-fluid analysis of flat heat pipes," *International Journal of Heat and Mass Transfer,* vol. 51, pp. 3113-3126, 2008.

[13] R. Ranjan, J. Y. Murthy, S. V. Garimella, and U. Vadakkan, "A numerical model for transport in flat heat pipes considering wick microstructure effects," *International Journal of Heat and Mass Transfer,* vol. 54, pp. 153-168, 2011.

[14] S. Chi, "Heat pipe theory and practice: a sourcebook," 1976.

[15] J. A. Weibel, S. V. Garimella, and M. T. North, "Characterization of evaporation and boiling from sintered powder wicks fed by capillary action," *International Journal of Heat and Mass Transfer,* vol. 53, pp. 4204-4215, 2010.

[16] Y.-T. Chen, J.-M. Miao, D.-Y. Ning, T.-F. Chu, and W.-E. Chen, "Thermal performance of a vapor chamber heat pipe with diamond-copper composition wick structures," in *2009 4th International Microsystems, Packaging, Assembly and Circuits Technology Conference*, 2009, pp. 340-343.

[17] T. Semenic and I. Catton, "Experimental study of biporous wicks for high heat flux applications," *International Journal of Heat and Mass Transfer,* vol. 52, pp. 5113-5121, 2009.

[18] Y. Zhao and C.-L. Chen, "An investigation of evaporation heat transfer in sintered copper wicks with microgrooves," in *ASME 2006 International Mechanical Engineering Congress and Exposition*, 2006, pp. 177-181.

[19] G. Hwang, Y. Nam, E. Fleming, P. Dussinger, Y. Ju, and M. Kaviany, "Multi-artery heat pipe spreader: Experiment," *International Journal of Heat and Mass Transfer,* vol. 53, pp. 2662-2669, 2010.

[20] G. Hwang, E. Fleming, B. Carne, S. Sharratt, Y. Nam, P. Dussinger, *et al.*, "Multi-artery heat-pipe spreader: Lateral liquid supply," *International Journal of Heat and Mass Transfer,* vol. 54, pp. 2334-2340, 2011.

[21] Z. Sun, X. Chen, and H. Qiu, "Experimental investigation of a novel asymmetric heat spreader with nanostructure surfaces," *Experimental thermal and fluid science,* vol. 52, pp. 197-204, 2014.

[22] J. A. Weibel, A. S. Kousalya, T. S. Fisher, and S. V. Garimella, "Characterization and nanostructured enhancement of boiling incipience in capillary-fed, ultra-thin sintered powder wicks," in *Thermal and Thermomechanical Phenomena in Electronic Systems (ITherm), 2012 13th IEEE Intersociety Conference on*, 2012, pp. 119-129.

[23] K.-S. Yang, T.-Y. Yang, C.-W. Tu, C.-T. Yeh, and M.-T. Lee, "A novel flat polymer heat pipe with thermal via for cooling electronic devices," *Energy Conversion and Management,* vol. 100, pp. 37-44, 2015.

[24] C. Li, G. Peterson, and Y. Wang, "Evaporation/boiling in thin capillary wicks (l)—Wick thickness effects," *Journal of Heat Transfer,* vol. 128, pp. 1312-1319, 2006.

[25] J. A. Weibel, S. S. Kim, T. S. Fisher, and S. V. Garimella, "Experimental characterization of capillary-fed carbon nanotube vapor chamber wicks," *Journal of Heat Transfer,* vol. 135, p. 021501, 2013.

[26] H. Zhang, Q. Pan, and H. Zhang, "Multi-scale porous copper foams as wick structures," *Materials Letters,* vol. 106, pp. 360-362, 2013.

[27] C. Ding, G. Soni, P. Bozorgi, B. D. Piorek, C. D. Meinhart, and N. C. MacDonald, "A flat heat pipe architecture based on nanostructured titania," *Journal of Microelectromechanical Systems,* vol. 19, pp. 878-884, 2010.

[28] Y. Nam, S. Sharratt, G. Cha, and Y. S. Ju, "Characterization and modeling of the heat transfer performance of nanostructured Cu micropost wicks," *Journal of Heat Transfer,* vol. 133, p. 101502, 2011.

[29] D. Ćoso, V. Srinivasan, M.-C. Lu, J.-Y. Chang, and A. Majumdar, "Enhanced heat transfer in biporous wicks in the thin liquid film evaporation and boiling regimes," *Journal of Heat Transfer,* vol. 134, p. 101501, 2012.

[30] S. Sharratt, C. Peng, and Y. S. Ju, "Micro-post evaporator wicks with improved phase change heat transfer performance," *International Journal of Heat and Mass Transfer,* vol. 55, pp. 6163-6169, 2012.

[31] Y.-T. Chen, S.-W. Kang, Y.-H. Hung, C.-H. Huang, and K.-C. Chien, "Feasibility study of an aluminum vapor chamber with radial grooved and sintered powders wick structures," *Applied Thermal Engineering,* vol. 51, pp. 864-870, 2013.

[32] J. S. Go, "Quantitative thermal performance evaluation of a cost-effective vapor chamber heat sink containing a metal-etched microwick structure for advanced microprocessor cooling," *Sensors and Actuators A: Physical,* vol. 121, pp. 549-556, 2005.

[33] Y. Peng, W. Liu, B. Liu, J. LIu, K. Huang, L. Wang, *et al.,* "The performance of the novel vapor chamber based on the leaf vein system," *International Journal of Heat and Mass Transfer,* vol. 86, pp. 656-666, 2015.

[34] Q. Cai and C.-L. Chen, "Design and test of carbon nanotube biwick structure for high-heat-flux phase change heat transfer," *Journal of Heat Transfer,* vol. 132, p. 052403, 2010.

[35] Q. Cai and A. Bhunia, "High heat flux phase change on porous carbon nanotube structures," *International Journal of Heat and Mass Transfer,* vol. 55, pp. 5544-5551, 2012.

[36] R. Ranjan, J. Y. Murthy, and S. V. Garimella, "Analysis of the wicking and thin-film evaporation characteristics of microstructures," *Journal of Heat Transfer,* vol. 131, p. 101001, 2009.

[37] K. A. Brakke, "The surface evolver," *Experimental mathematics,* vol. 1, pp. 141-165, 1992.

[38] J. Hilden and K. Trumble, "Numerical analysis of capillarity in packed spheres: Planar hexagonal-packed spheres," *Journal of colloid and interface science,* vol. 267, pp. 463-474, 2003.

[39] J. D. Bernardin, I. Mudawar, C. B. Walsh, and E. I. Franses, "Contact angle temperature dependence for water droplets on practical aluminum surfaces," *International journal of heat and mass transfer,* vol. 40, pp. 1017-1033, 1997.

[40] Y. Nam, S. Sharratt, C. Byon, S. J. Kim, and Y. S. Ju, "Fabrication and characterization of the capillary performance of superhydrophilic Cu micropost arrays," *Journal of Microelectromechanical Systems,* vol. 19, pp. 581-588, 2010.

[41] J. C. Maxwell, *A treatise on electricity and magnetism* vol. 1: Clarendon press, 1881.

[42] D. Reay, R. McGlen, and P. Kew, *Heat pipes: theory, design and applications*: Butterworth-Heinemann, 2013.

[43] A. C. Technologies, "Merit Number And Fluid Selection."

[44] T. E. ToolBox, "Thermal Conductivities for some common Liquids."

[45] M. T. Ababneh, S. Chauhan, F. M. Gerner, D. Hurd, P. de Bock, and T. Deng, "Charging Station of a Planar Miniature Heat Pipe Thermal Ground Plane," *Journal of Heat Transfer,* vol. 135, p. 021401, 2013.

[46] M. Gao, Y. Cao, W. K. Jones, and M. A. Zampino, "Ceramic miniature heat pipes and liquid charging methods," *ASME-PUBLICATIONS-HTD,* vol. 366, pp. 429-434, 2000.

[47] C. Li, Y. Luo, C. Zhou, Q. Shan, and X. Wang, "Using peristaltic pump to charge micro heat pipe for high-power LED," in *Nano/Micro Engineered and Molecular Systems (NEMS), 2015 IEEE 10th International Conference on*, 2015, pp. 164-167.

[48] Y. Yadavalli, J. A. Weibel, and S. V. Garimella, "Flat heat pipe performance thresholds at ultra-thin form factors," in *Thermal and Thermomechanical*

Phenomena in Electronic Systems (ITherm), 2014 IEEE Intersociety Conference on, 2014, pp. 527-534.

[49] R. Ranjan, J. Y. Murthy, S. V. Garimella, D. H. Altman, and M. T. North, "Modeling and design optimization of ultrathin vapor chambers for high heat flux applications," *IEEE Transactions on Components, Packaging and Manufacturing Technology*, vol. 2, pp. 1465-1479, 2012.

[50] A. D. Kraus and A. Bar-Cohen, "Thermal analysis and control of electronic equipment," *Washington, DC, Hemisphere Publishing Corp., 1983, 633 p.*, vol. 1, pp. 76-79, 1983.

[51] T. Inc., "DATASHEET – THERMA-BASE™ Vapor Chamber."

[52] M. Ababneh, "Novel Charging Station and Computational Modeling for High Thermal Conductivity Heat Pipe Thermal Ground Planes," University of Cincinnati, 2012.